Electrical Excitation of Surface Plasmon Polaritons

Cover: artist impression of electrically excited surface plasmon polaritons in a metal–insulator–metal geometry.

Ph.D. Thesis Utrecht University, February 2009
Electrical Excitation of Surface Plasmon Polaritons
Rob van Loon

ISBN 978-90-77209-31-8

A digital version of this thesis can be downloaded from http://www.amolf.nl.

Electrical Excitation of Surface Plasmon Polaritons

Elektrische Excitatie van Oppervlakteplasmonpolaritonen

(met een samenvatting in het Nederlands)

Proefschrift

ter verkrijging van de graad van doctor aan de Universiteit Utrecht
op gezag van de rector magnificus, prof. dr. J. C. Stoof,
ingevolge het besluit van het college voor promoties
in het openbaar te verdedigen
op woensdag 25 februari 2009 des middags te 12.45 uur

door

Rob Victor Alouisius van Loon

geboren op 7 april 1981 te Bergen op Zoom

Promotor: Prof. dr. A. Polman

The work described in this thesis was part of the research program of the 'Stichting voor Fundamenteel Onderzoek der Materie' (FOM), which is financially supported by the 'Nederlandse organisatie voor Wetenschappelijk Onderzoek' (NWO). This work was also supported by the NanoNed technology program of the Dutch Ministry of Economic affairs.

All that glisters is not gold.

[The merchant of Venice (II, vii), William Shakespeare]

Contents

Chapter 1

General introduction

1.1 Surface plasmon photonics

A surface plasmon polariton (SPP) is an electromagnetic wave propagating at the interface between a metal and a dielectric material that is coupled to a charge density oscillation of the free electrons at the surface of the metal [1, 2]. Because SPPs are bound to the interface and their electric field decays exponentially perpendicular to the interface, SPPs are essentially 2-dimensional waves. This confinement and concentration of the electromagnetic field makes SPPs interesting for a wide range of applications [3–6]. The two-dimensional confinement enables the realization of optical components with small dimensions in the out-of-plane direction [7, 8]. Furthermore, because of the strong coupling with the electrons, the dispersion of SPPs can be tuned to a degree that cannot be achieved with dielectrics.

Figure 1.1 shows the dispersion relation for SPPs at the silver/air interface (solid line). The dispersion relation shows the in-plane k-vector ($k = 2\pi/\lambda$, with λ the SPP wavelength) as a function of the optical frequency. The dispersion in air is plotted as reference (dash-dotted line). By engineering the metal geometry, the SPP dispersion can be tuned [9]. As an example, figure 1.1 also shows the dispersion for an SPP waveguide composed of two parallel metal planes separated by a dielectric layer (dashed lines). By varying the dielectric layer thickness, the coupling between the plasmons on either side, and hence the dispersion can be tuned. As can be seen in figure 1.1 near the surface plasmon resonance indicated by the dotted line, very high wave vectors and thus short wavelengths can be achieved. In this way, the wavelength can be shrunk more than ten-fold, compared to the free space wavelength [10]. This enables the design of integrated optical components and circuits at length scales below 100 nm. By confinement of SPPs in taper geometries [11, 12] light can be even further concentrated at length scales that approach the true nanoscale. Such geometries enable applications in surface plasmon sensing by using e.g. Raman spectroscopy.

1.2 Exciting surface plasmon polaritons

As can be seen in figure 1.1, the dispersion of SPPs lies right from the light line, outside the reach of momenta that can be obtained by photons at the corresponding frequencies. The momentum mismatch between a photon and a plasmon can be overcome by applying a prism coupling technique, as is shown in figure 1.2, which shows the Kretschmann prism coupling configuration [1]. A thin metal layer deposited on a prism supports SPP modes on its top side. A

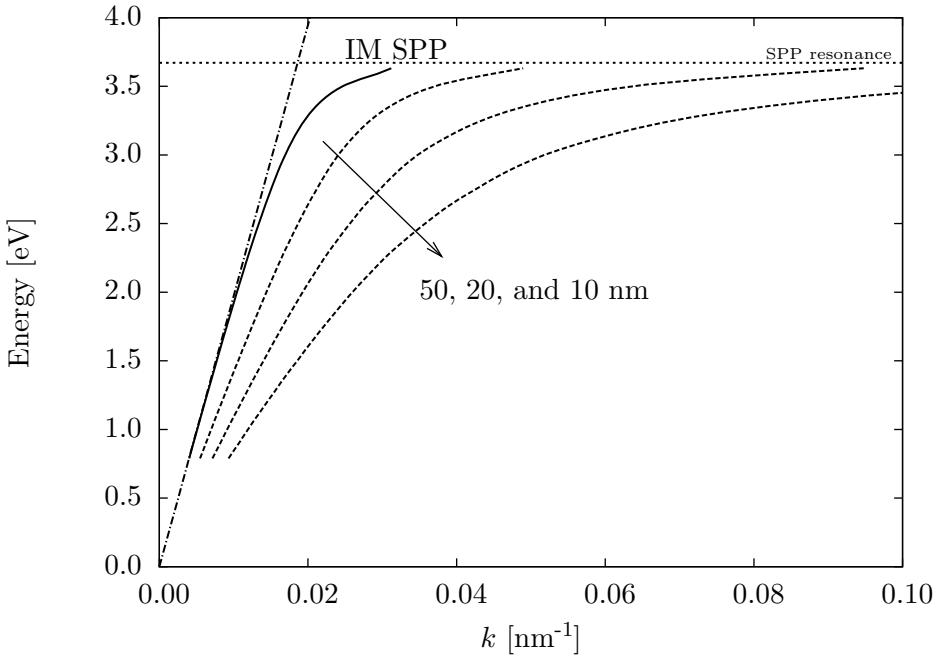

Figure 1.1: Dispersion relation of a surface plasmon polariton (solid line), at the Ag/air interface and the light line in air (dash-dotted line). The dashed lines show the dispersion relation for an SPP in a metal–insulator–metal geometry, for which the insulator thickness is varied. The surface plasmon resonance for Ag at 3.7 eV is indicated by the dotted line.

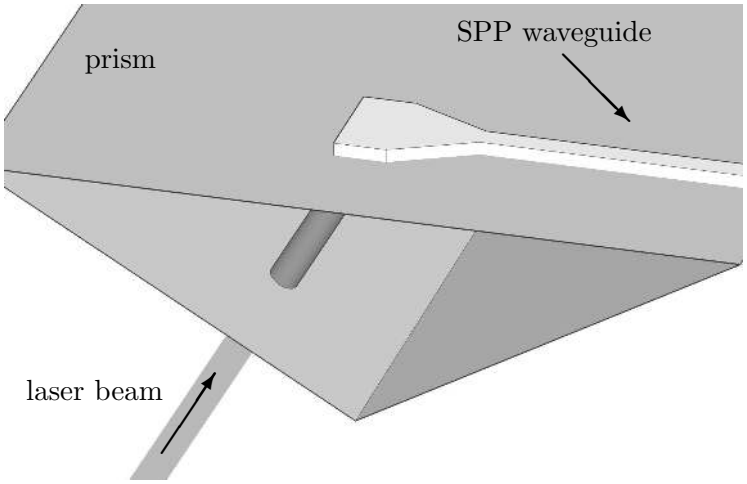

Figure 1.2: Schematic of excitation of SPPs by a prism coupling technique. A laser beam is incident on a prism. The light penetrates into the metal layer and excites SPPs on the top side of the metal, which then can propagate into a plasmon waveguide.

laser beam is incident on the rear side through the prism. SPPs on the metal surface are then excited by matching the wavelength of SPPs and incident beam in the glass, by optimizing the incident angle. Surface plasmon resonance sensors that sense small variations in refractive index in a liquid put on top of the metal often make use of this SPP excitation mechanism [13].

An alternative far-field excitation technique for SPPs is based on grating coupling [1] in which a laser beam is focused onto a grating and SPPs are generated. Figure 1.3 shows a schematic of this SPP excitation grating coupling technique. Both the prism and grating coupling technique are rather bulky geometries and are therefore impractical for the use in small integrated circuits or sensors. Also, the requirement of a (bulky) laser for excitation is a disadvantage. In this thesis we present an entirely new concept for the generation of SPPs by an electrical injection method that solves these problems.

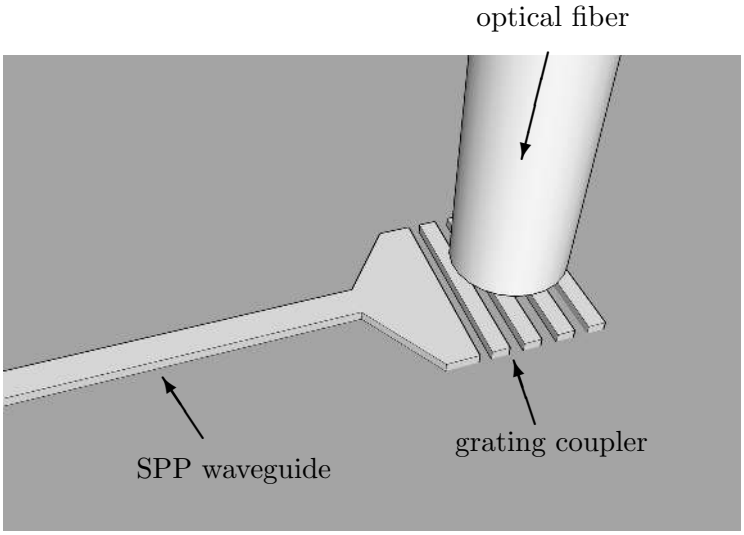

Figure 1.3: Schematic of excitation of SPPs by a grating coupling technique. Light is incident through an optical fiber positioned close to a grating [14] and excites SPPs that propagate over a metallic waveguide.

1.3 Electrical SPP source

While the excitation of SPPs by prisms or grating coupling is done by a far-field radiation source, SPPs can also be excited by near-field interactions [15–19]. In this thesis we introduce the excitation of SPPs by silicon quantum dots that are placed in the optical near-field of a metal nanostructure that supports SPPs. The quantum dots are electrically excited, and decay by the excitation of SPPs. The near-field coupling between the quantum dots and the metal/dielectric interfaces represents a broad range of k-vectors that overlap with the dispersion curve in figure 1.1.

Figure 1.4 shows a schematic of the device layout. A dielectric material that is sandwiched between two metal layers is doped with Si quantum dots. The metal layers are spaced by 50–100 nm and serve both as a plasmon waveguide and as electrical contacts. This SPP source has several advantages over SPP excitation mechanisms based on far-field coupling techniques that use a prism or a grating. The excitation source of SPPs by quantum dots can be scaled to very small dimensions and can be positioned on a desired po-

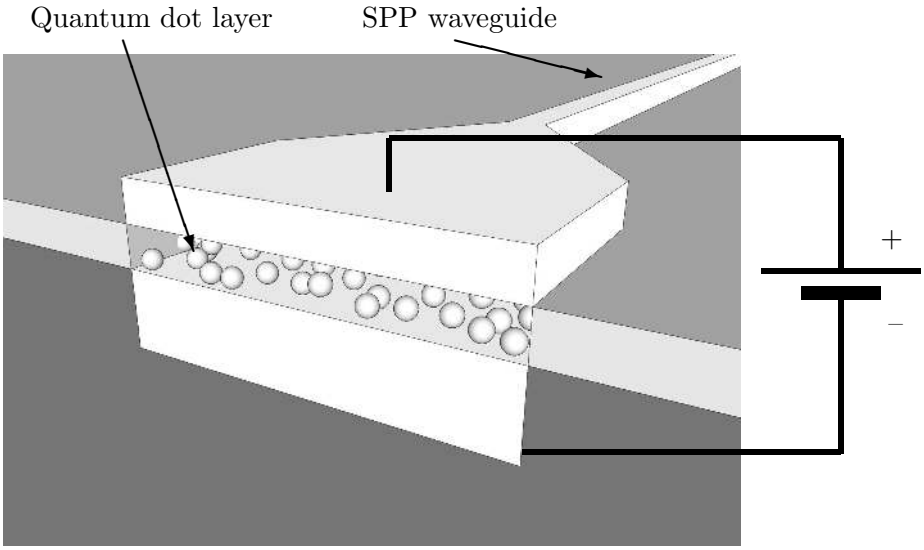

Figure 1.4: Schematic device layout of an integrated electrical source for SPPs, as demonstrated in this thesis. A dielectric layer doped with Si quantum dots (depicted as spheres) is sandwiched between two metal layers, which serve both as electrical contact and as SPP waveguide. The SPPs propagate in plane, between the two metal layers.

sition on the chip. By suitable engineering of the optical waveguide design, the SPP source does not need to be at the top side of the device, as is necessary for systems based on the far field excitation of SPPs, but can also be integrated in depth if required. Parallel to our work, an SPP source based on an organic light emitting diode (OLED) has been recently demonstrated by Koller *et al.* [17]. Our work is complementary to these results and focuses on compatibility with standard CMOS fabrication techniques for integrated circuits.

1.4 Contents of this thesis

Chapter 2 describes the luminescence properties of Si quantum dots in silica. Silicon quantum dots are small crystalline clusters (diameter < 5 nm) of Si atoms that show quantum confined luminescence at room temperature. Luminescence spectra under optical excitation, electrical excitation, and excitation

by a high energy electron beam are presented. The spectrally resolved decay rate of the Si quantum dots under optical excitation is measured and an estimate is derived for the optical excitation cross section.

Chapter 3 presents an electrical source for SPPs based on an insulator–metal–insulator (IMI) geometry, doped with Si quantum dots. We study the near-field coupling between quantum dots and SPPs and find an optimized design for the generation of SPPs. We describe the fabrication of the SPP source and present measurements that show evidence of electrical excitation of SPPs. Based on the same geometry an IMI SPP source operating in the infrared region was fabricated by incorporating erbium in the dielectric material.

Chapter 4 describes the optical and electrical properties of Si quantum dots embedded in thin alumina films. These layers form the active region in an electrical metal–insulator–metal (MIM) plasmon source. Both photoluminescence and electroluminescence are studied.

The MIM plasmon source is described in chapter 5. A novel device geometry based on a thin MIM membrane made in a Si wafer is introduced. SPPs are electrically excited across the MIM membrane and are guided into a waveguide structure with integrated outcoupling structures. By detecting light in the far-field in a range of designs, the electrically excitable SPP source is demonstrated.

Finally, chapter 6 describes the application prospects of the electrical SPP source described in this thesis in diverse areas, such as sensing, photovoltaics, and opto-electronic integration.

Chapter 2

Optical properties of silicon nanocrystals in a silica matrix

This chapter discusses the characterization of Si nanocrystals in a silica matrix. SiO_x layers were deposited by a magnetron sputtering process of silicon in an oxide atmosphere. A thermal anneal step after the deposition, converts the SiO_x material into an SiO_2 layer doped with Si nanocrystals. The nanocrystals show quantum confined photoluminescence with a peak wavelength of $\lambda = 800$ nm. Electroluminescence is observed in the $\lambda = 550$–750 nm range under 15–30 V bias. Samples co-doped with erbium show electroluminescence at $\lambda = 1.5$ μm. The effect of electron beam irradiation (0.5–20 keV) on photoluminescence is studied: strong bleaching is observed for electron doses > 150 $\mu C/cm^2$.

2.1 Introduction

Silicon is the key element in the semiconductor industry. During the last decades, there has been an enormous knowledge built up on how to process silicon and how to fabricate electronic components of silicon. Light emitting components however, are difficult to fabricate from silicon. Because silicon as a bulk material has an indirect band gap [20], the radiative decay rate is low compared to the non-radiative rate. By using special fabrication techniques, the highest reported efficiency of a silicon light emitting diode is 1% [21].

By using silicon nanocrystals instead of bulk silicon, it is possible to modify the electronic band structure in the material and thereby blueshift the band gap with respect to the bulk band gap (1100 nm) [22]. By tuning the size of the nanocrystals, the color of the emitted light can thus be controlled [23, 24]. For Si nanocrystals, the diameter is in the range of 2–5 nm [25–27]. The peak intensity lies in the range of $\lambda = 700$ to 900 nm and the width of the spectrum is typically 200 nm full width at half maximum (FWHM). While photoluminescence of Si quantum dots is quite often reported, the reports on electroluminescence of Si quantum dots are limited [e.g. 28–32].

2.2 Fabrication

There exist several host materials for Si nanocrystals. The most common host matrix is silica. There are also reports on Si nanocrystals in silicon-nitride [33]. Chapter 4 of this thesis discusses Si nanocrystals in alumina. The fabrication techniques for Si nanocrystals range from Si^+ ion-implantation [34], chemical vapor deposition [27, 35], pulsed-laser ablation [36], to sputtering [37]. It is also possible to fabricate Si nanocrystals by using wet chemical synthesis [38], or by using sol-gel precursors [39].

The nanocrystals discussed in this thesis (chapters 2 and 3) are fabricated by magnetron sputtering of a Si target in an oxide atmosphere. This deposition was done in the group of Prof. Dr. R. E. I. Schropp at Utrecht University. This fabrication technique was chosen, because the stoichiometry of the deposited film can be controlled while depositing the film. In our case this results in a continuous and homogenous distribution of excess Si in the silica layer.

As a substrate, a silicon on insulator (SOI) wafer was used. It was cleaned using sonication in de-mineralized water, followed by a standard RCA cleaning process [40] of a 15 minute soak in a mixture of de-mineralized water, ammonia, and hydrogen peroxide at 70 °C. After this cleaning process, a substoichiometric oxide film (SiO_x, with $x < 2$) was then deposited using magnetron

sputtering of silicon in an oxygen atmosphere. By regulating the oxygen pressure, the stoichiometry of the deposited silica film is controlled in situ. Details about the SiO_x deposition process can be found in reference [37]. To convert the SiO_x layer into a silica layer doped with Si nanocrystals, the sample was annealed in a rapid thermal anneal furnace at 1000 °C for 10 minutes in an argon atmosphere [41]. Subsequently, the sample was passivated for 30 minutes at 800 °C in a forming gas atmosphere (a mixture of 80% nitrogen and 20% hydrogen gas). Hydrogen from the forming gas diffuses into the sample and passivates Si dangling bonds [34].

2.3 Refractive index

The refractive index of the as-deposited layer and the annealed layer are measured using a variable angle spectroscopic ellipsometer. Figure 2.1 shows the real part of the refractive index $N = n+ik$; figure 2.2 shows the imaginary part of the refractive index. The refractive indices of both the as-deposited and the annealed films are, as expected, in between the literature values of SiO_2 [42] and SiO [43]. The refractive index of the annealed film is slightly lower than the index of the as-deposited layer, which might be due to a decrease in Si volume fraction [44].

The two figures 2.1 and 2.2 also show an effective medium approximation based on the Maxwell Garnett model. This approximation models the dielectric constant as a combination of a guest and a host material as [45]:

$$\frac{\epsilon - \epsilon_h}{\epsilon + 2\epsilon_h} = f\frac{\epsilon_g - \epsilon_h}{\epsilon_g + 2\epsilon_h}, \tag{2.1}$$

where ϵ is the effective dielectric constant, $\epsilon_{h,g}$ the dielectric constant of the host and the guest material, and f is the volume fraction of the guest material. The approximation shown in figures 2.1 and 2.2 uses SiO_2 as host with 10% Si as guest material. The calculation for n is in agreement with the measured trend, while the calculation for k does not give the enhanced absorption between λ = 400–600 nm that is seen in the experiment. The latter is ascribed to a defect in the SiO_x layers.

2.4 Photoluminescence

Figure 2.3 shows a photoluminescence (PL) spectrum of the Si nanocrystal doped oxide layer. The SiO_x layer ($x = 1.3$) was 150 nm thick. The nanocrystals were excited using the 488 nm line of an argon-ion laser. The light

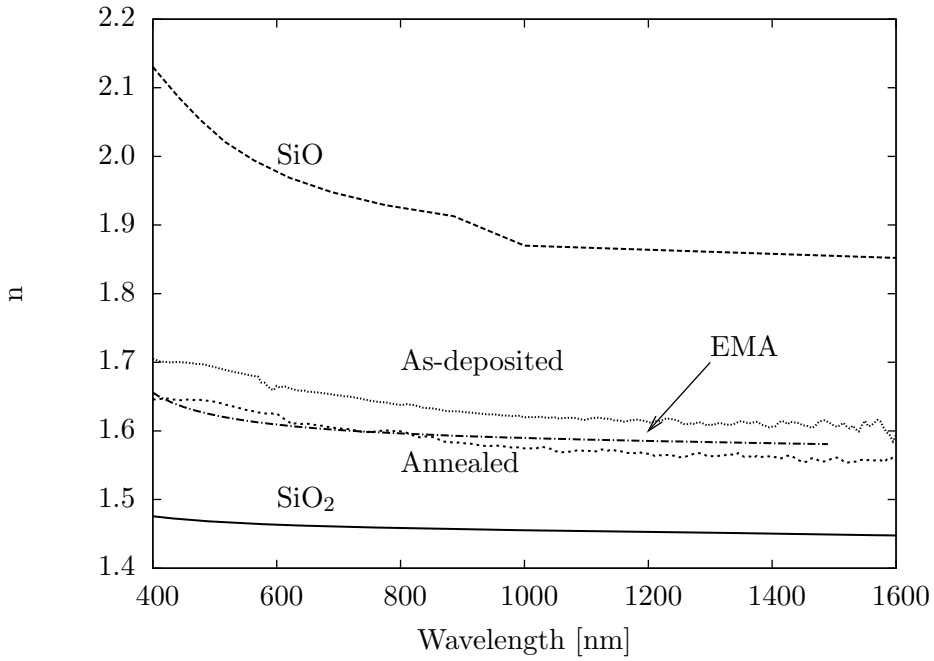

Figure 2.1: Real part of the refractive index of $N = n + ik$ for an as-deposited and an annealed SiO_x film (150 nm thick, $x = 1.6$). The refractive indices of SiO_2 and SiO are shown as reference. An effective medium approximation (EMA) based on the Maxwell Garnett model with 10% Si in SiO_2 is shown as well.

emitted by the nanocrystals was collected with a $f = 2.5$ cm lens (NA = 0.45). A spectrograph with a Si CCD-detector measured the spectrum. In order to separate the luminescence of the sample from the excitation laser, a low-pass filter was placed in front of the entrance slits of the spectrograph. The PL spectrum peaks at $\lambda = 780$ nm, corresponding to a nanocrystal diameter of 3 nm [26]. The FWHM of the spectrum is 150 nm.

The PL intensity of the Si nanocrystals after switching on (pump up trace) and switching off (decay trace) of the excitation laser was measured temporally- and spectrally-resolved. The pump was switched on/off by using an acousto-optic modulator (AOM). The measured rise/fall time of the AOM was on the order of 50 ns (system response). The PL of the Si nanocrystals was spectrally resolved by a monochromator and detected by a photo-multiplier tube (PMT). A multichannel-scaler measured the time-resolved PL intensity.

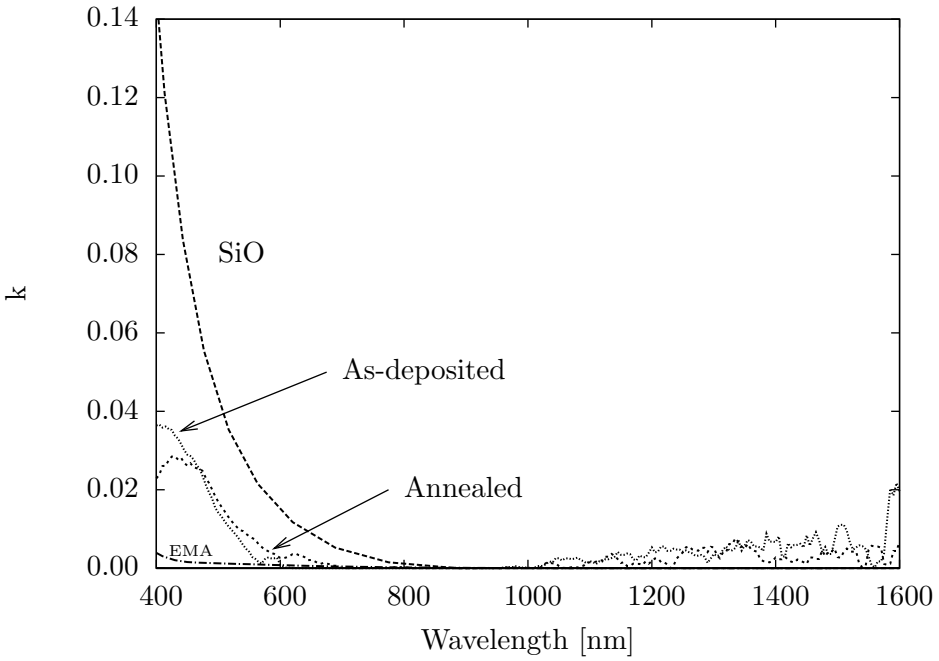

Figure 2.2: Imaginary part of the refractive index of $N = n + ik$ for an as-deposited and an annealed SiO_x film (150 nm thick, $x = 1.6$). The refractive indices of SiO_2 and SiO are shown as reference. An effective medium approximation (EMA) based on the Maxwell Garnett model with 10% Si in SiO_2 is shown as well.

Figure 2.4 shows a typical decay trace of Si nanocrystals in SiO_2 for the same sample as in figure 2.3. This decay trace was measured at $\lambda = 800$ nm. The laser was switched off at $t = 230$ µs. A fit to the data is also plotted. The fit-function was a stretched exponential decay function [46]:

$$I(t) = Ae^{-\left(\frac{t-t_0}{\tau}\right)^{\beta}} + B, \tag{2.2}$$

where I is the PL intensity at time t, A the nanocrystal PL intensity before switching off the excitation laser at time t_0, τ the lifetime, β the "stretch factor", and B the background due to dark counts in the PMT. Equation 2.2 is based on a model that assumes there is a distribution of decay rates. The lifetime τ and the stretch factor β determine the most frequent decay rate and the width of the decay rate distribution. A similar expression was used to fit

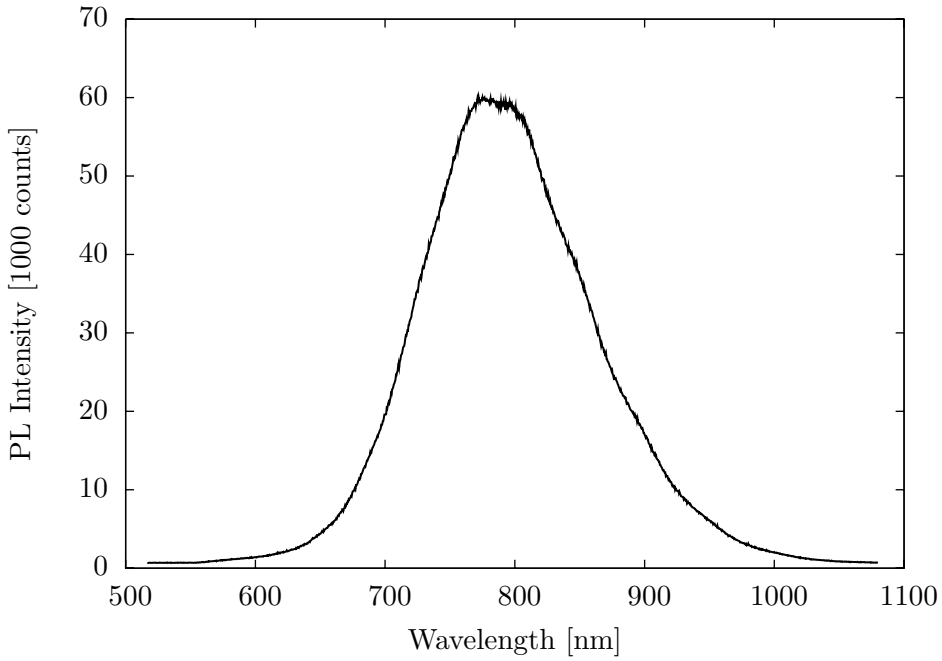

Figure 2.3: Photoluminescence spectrum of an SiO_2 layer doped with Si nanocrystals fabricated by magnetron sputtering of SiO_x followed by annealing. The nanocrystals were excited using the 488 nm line of an argon-ion laser (6.5 W/cm^2). The exposure time was 0.5 seconds.

to the measured switch-on trace. The time offsets (t_0) were set to 30 µs (rise time offset) and 230 µs (decay time offset). The fit to the data was then based on six parameters: $A, \tau_{\text{rise}}, \beta_{\text{rise}}, \tau_{\text{decay}}, \beta_{\text{decay}}$, and B. The inset of figure 2.4 shows the entire time trace, including the switch-on trace.

Time traces as in figure 2.4 were measured for the entire PL spectrum of the Si nanocrystals, with a wavelength-step of $\Delta\lambda = 20$ nm. The passband of the monochromator was 43 nm. Figure 2.5 shows the fitted rise time (□) and the fitted decay time (●). The error bars denote the 90% confidence level of the fit. These decay times agree with typical values found in literature [e.g. 23, 32, 47, 48]. The fitted β for the decay traces increases for larger wavelengths ($\beta = 0.4$ at $\lambda = 650$ nm to $\beta = 0.7$ at $\lambda = 900$ nm). The fitted β for the rise time traces follows the same trend as the β for the decay curves.

The decay times for Si nanocrystals increase for longer wavelengths (figure 2.5). This increase has two causes. First the lifetime of nanocrystals

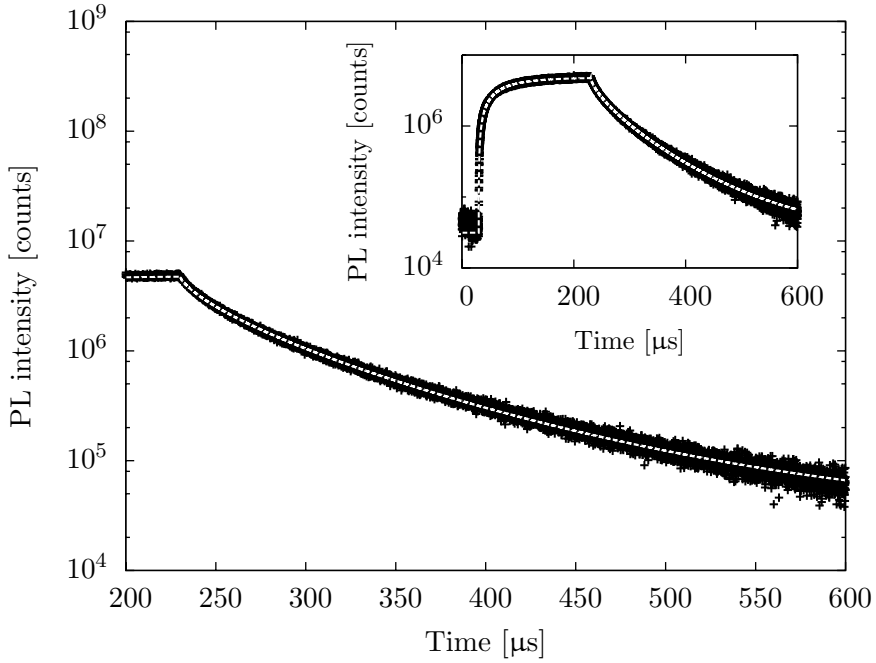

Figure 2.4: Photoluminescence decay trace of Si nanocrystals at $\lambda = 800$ nm after switching off the pump laser. A stretched exponential fit to the data is also plotted. The fit parameters (see equation 2.2) are: $A = 4.37 \times 10^6$ counts, $\tau_{\text{decay}} = 37.1$ µs, $\beta_{\text{decay}} = 0.7$, and $B = 3.14 \times 10^4$ counts. The inset shows the entire time trace, including the switch-on trace.

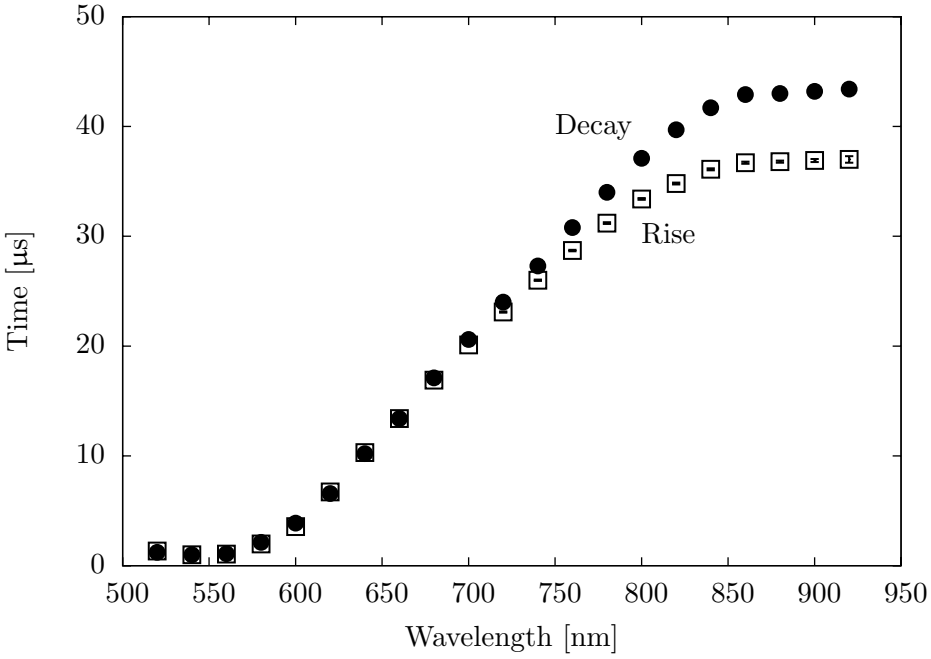

Figure 2.5: Rise time τ_{rise} (□) and decay time τ_{decay} (●) from fits to measurements as in figure 2.4, as a function of wavelength. The error bars are smaller than the symbol size and denote the 90% confidence level of the fit.

that emit more to the red side of the spectrum (i.e. larger nanocrystals) have a smaller radiative exciton decay rate [47, 49, 50] due to the lower degree of quantum confinement. Secondly, the lifetime is increased in the red part of the spectrum due to the smaller optical density of states (that scales with ω^2) [51]. The smaller β-factor found for the smallest wavelength is ascribed to a larger inhomogeneity in energy transfer paths for the smaller nanocrystals [48].

Combining the data on τ_{rise} and τ_{decay} gives information about the excitation cross section. For low-power excitation, the excitation rate $1/\tau_{\text{rise}}$ equals the pump power times the excitation cross section plus the decay rate $1/\tau_{\text{decay}}$ [32]:

$$\frac{1}{\tau_{\text{rise}}} = \sigma\phi + \frac{1}{\tau_{\text{decay}}}, \tag{2.3}$$

where σ is the excitation cross section and ϕ the pump laser photon flux. To take into account the distribution of decay rates described by β, we have used the average decay times given by [52]:

$$\langle\tau\rangle = \frac{\tau}{\beta}\Gamma\left(\frac{1}{\beta}\right), \tag{2.4}$$

where Γ is the gamma function and τ is lifetime (τ_{on} or τ_{off}). The excitation power and the pump spot size were kept constant for the entire measurements series, leading to a constant excitation photon flux on to order of $\phi = 6.5$ W/cm^2. We find that the cross section increases from $\sigma = 1.9 \times 10^{-16}$ cm^2 at $\lambda = 700$ nm to $\sigma = 3.5 \times 10^{-16}$ cm^2 at $\lambda = 900$ nm. These values are in agreement with PL excitation cross section found by Kovalev *et al.* [53].

2.5 Electroluminescence

To achieve electroluminescence from Si nanocrystals, the following procedure was used. The SiO_x layer was deposited onto an SOI wafer (see section 2.2). During deposition, a part of the substrate was covered by a physical mask, leaving it accessible for electrical contacting. By using electron beam lithography, physical vapor deposition, and lift-off, gold contacts were fabricated on the bare silicon device layer of the substrate and on the deposited SiO_x layer. The samples were annealed and passivated as described above, before the electric contacts were made. The samples were mounted onto a printed circuit board and the electric contacts were made by wire bonding. The left

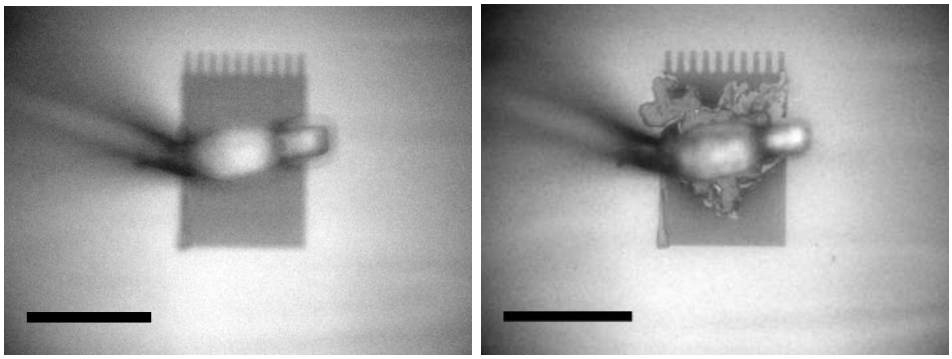

Figure 2.6: Gold patch as an electrical contact on the SiO_x film before (left), and after (right) the electroluminescence measurements. The scale bar is 100 µm.

panel of figure 2.6 shows an optical microscope image of the electrical contact on the SiO_x with the wire bond.

An electrically contacted sample (150 nm of SiO_x, with $x = 1.3$) was mounted under an inverted scanning confocal microscope. A voltage source was used to bias the sample, where the contact on the SiO_x was positively biased. The Si nanocrystals were excited by impact excitation [28]. EL spectra for several different biasing conditions are shown in figure 2.7. For higher biasing voltages –and thereby larger currents– the EL spectra increased in intensity and the spectra showed a blueshift. Both effects have been previously reported [28, 54] and can be explained by the impact excitation model. For a higher voltage, the inserted electrons have more energy and can excite smaller nanocrystals and thus create a blueshift in the spectrum. Instead of a homogeneous distribution of electroluminescence, the light emission was dominated by hotspots, that eventually deteriorated the gold contact (see figure 2.6).

The spectra in figure 2.7 show Fabry–Pérot fringes [55] with a free spectral range of 665 cm^{-1} that are independent of biasing conditions. These fringes are due to interference in the 5 µm thick buried oxide layer of the SOI-wafer.

2.6 Bleaching by electron beam irradiation

Electron beam lithography was used to fabricate nanostructures, as will be discussed further. It must be known what the effect of electron irradiation of the nanocrystals PL is. To study this, we have performed cathodoluminescence

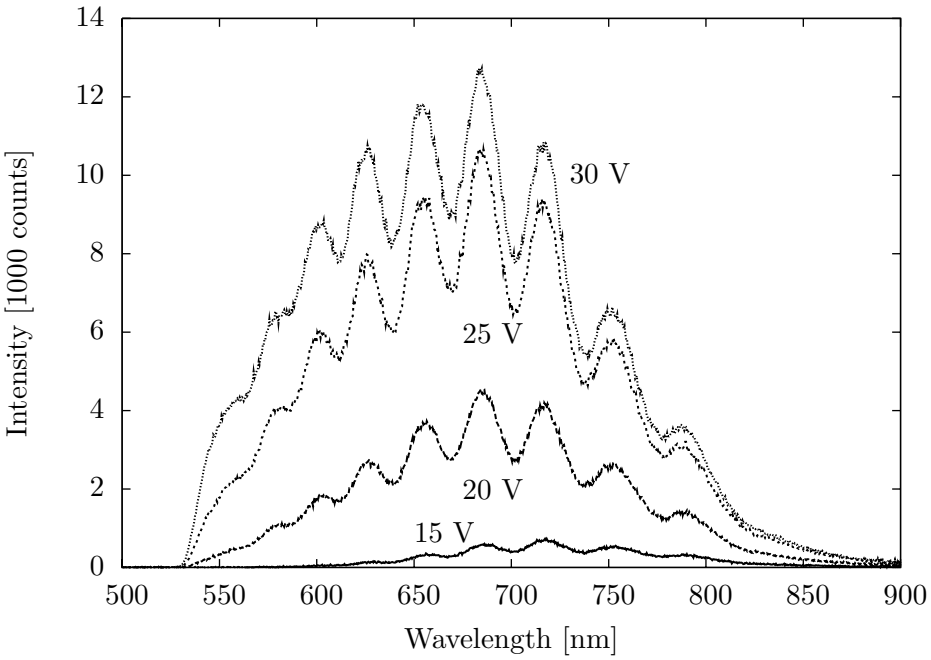

Figure 2.7: Electroluminescence spectra taken from the sample from figure 2.6 for several different biasing conditions (15 V: 7.2 mA, 20 V: 9.76 mA, 25 V: 12.3 mA, 30 V: 14.83 mA). For larger biasing conditions, the spectra increased in intensity and show a blueshift. The fringes in the spectra originate from interference in the buried oxide layer of the SOI substrate.

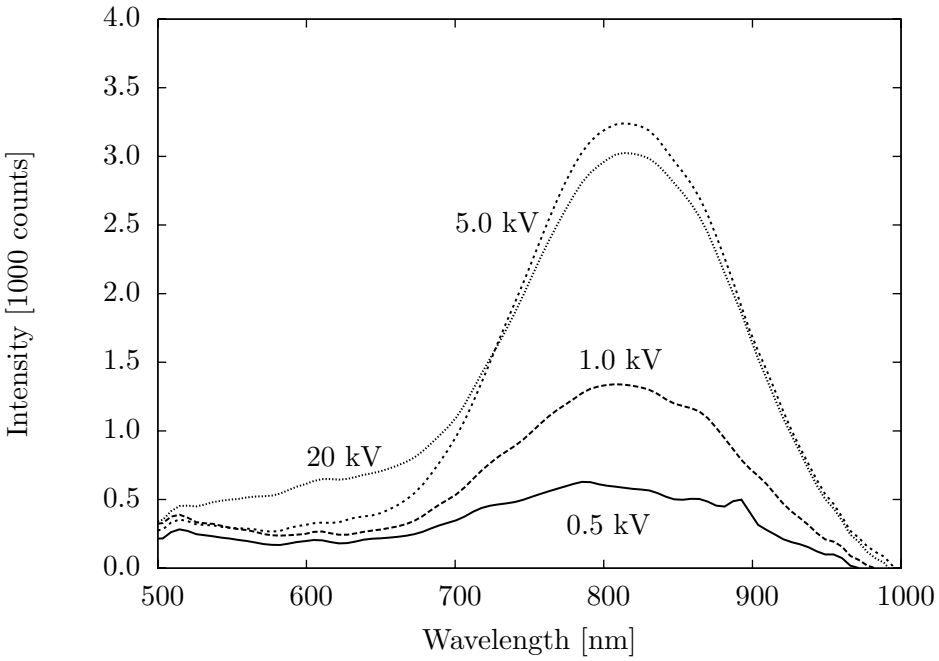

Figure 2.8: Cathodoluminescence spectra of Si nanocrystals (50 nm of SiO_x, with $x = 1.1$) for several different electron acceleration energies. The exposure time was 100 s. The area scanned by the electron-beam was 460×350 µm.

(CL) spectroscopy inside a scanning electron microscope (SEM), where a high energy electron beam excited the Si nanocrystals [56, 57]. Light emitted by the sample, when the electron beam of an SEM is scanned over the structure, is collected by a parabolic mirror and is directed to a spectrometer. A small hole in the parabolic mirror allows the electron beam to pass. A detailed explanation of the CL set-up can be found in reference [58].

Figure 2.8 shows CL spectra for several different electron energies on a Si nanocrystal doped SiO_2 layer (50 nm of SiO_x, with $x = 1.1$, annealed and passivated as described above). The CL spectra peak at around $\lambda = 820$ nm and the width is 200 nm FWHM. Each measurement was performed on a separate position on the sample. The exposure time for the spectrum was 100 s. The area scanned by the electron beam was 460×350 µm. The electron beam current at each electron energy is given in table 2.1.

During the electron beam exposure, the Si nanocrystals bleached: the lu-

Table 2.1: Electron beam currents and average deposited energy for different electron energies.

Energy [kV]	Current [nA]	Average deposited energy [eV/nm/electron]
0.5	5.21	10
1.0	10.3	20
5.0	14.9	15
20	32.7	3.6

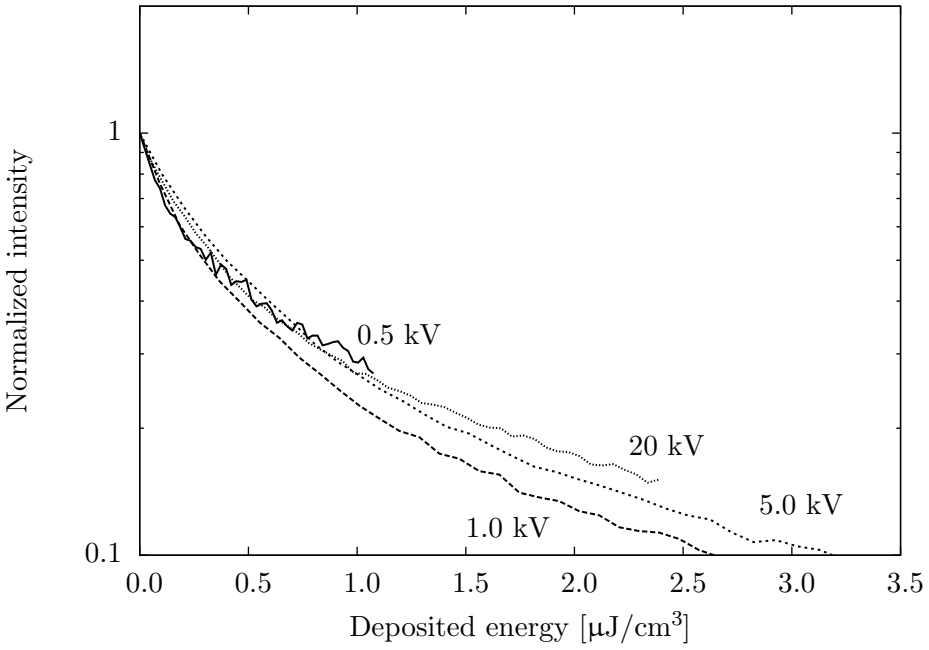

Figure 2.9: Cathodoluminescence intensity of Si quantum dots in SiO_2 as a function of deposited energy. The integrated luminescence intensity between λ = 750–850 nm is plotted, normalized at 0 fluence.

minescence intensity decreased for longer electron-beam exposures and it did not recover afterwards. Figure 2.9 shows the decrease of normalized luminescence intensity between $\lambda = 750$–850 nm as a function of the deposited energy during a 100 s exposure to the electron beam for the four electron energies. The deposited energy is estimated based on Monte Carlo simulations [59].

When normalized to deposited energy, all measurement follow a similar trend. The $1/e$-dose for the luminescence decay was in the range of 150 to 400 $\mu C/cm^2$, depending on the electron beam energy. This bleaching dose is comparable to the dose required for electron beam lithography [60], leaving this fabrication technique unsuitable to define nano- and micro-scale structures that are composed of Si nanocrystals.

2.7 Erbium co-doped SiO_x layers

Erbium ions are of great interest in optoelectronic research, due to their intra-4f emission at 1.54 μm. This is a standard telecom wavelength, because of the low loss of optical fibers at this wavelength. To overcome the problems associated with the low cross section of erbium (on the order of 10^{-21} to 10^{-20} cm^2 [61]), Si nanocrystals can be used as sensitizers [48, 62]. Here we use the SiO_x material made by magnetron sputtering of Si (see section 2.2) and use an additional ion-implantation to incorporate erbium into the SiO_x film. After the deposition of the SiO_x film (150 nm of SiO_x, with $x = 1.3$), a layer of 50 nm of Si was deposited by the same method onto the SiO_x film. Erbium ions were implanted with an energy of 300 keV into the SiO_x layer to a fluence of 5×10^{15} cm^{-2}, leading to a peak concentration of 1 at.% at 120 nm from the top interface (which is the middle of the SiO_x film) [59]. Subsequently, boron-ions were implanted with an energy of 5 keV into the top Si layer to a fluence of 3×10^{13} cm^{-2} to increase the electrical conductivity of this layer. To form the Si nanocrystals and to activate the Er, a one hour anneal at 900 °C in an argon atmosphere was performed. Electrical contacts were made by electron beam lithography, physical vapor deposition, and lift-off. The samples were mounted onto a printed circuit board and the electrical contacts were made by wire bonding (see section 2.5).

Electroluminescence measurements were done in a similar fashion as described in section 2.5. The EL was measured by a spectrometer with an infrared-sensitive InGaAs photodiode array. Figure 2.10 shows an EL emission spectrum of erbium with a typical emission peak at $\lambda = 1540$ nm. The collection time was five minutes. As the electrical contacts in these samples

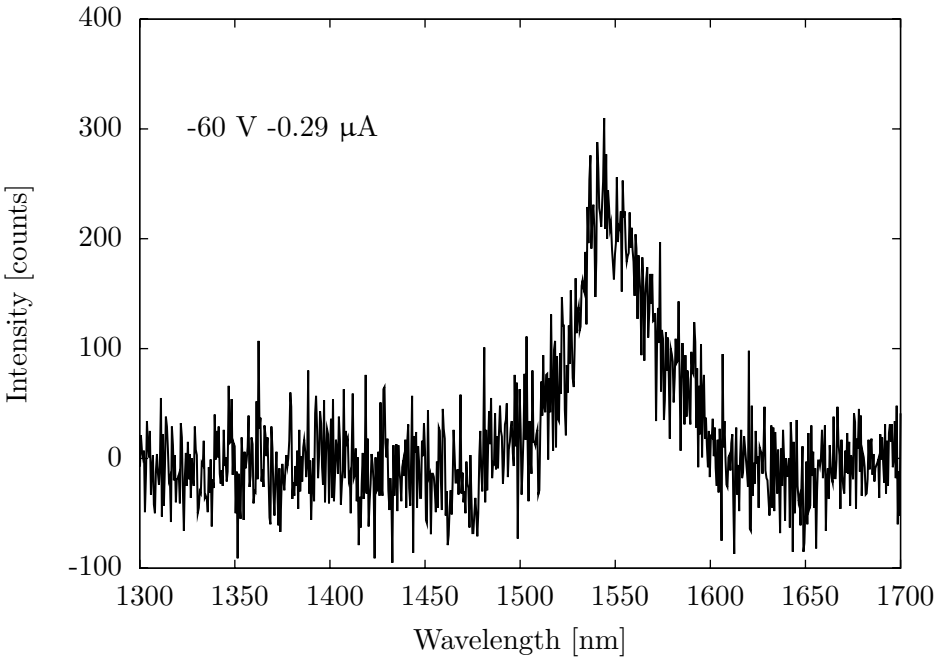

Figure 2.10: Electroluminescence of 150 nm thick SiO_x ($x = 1.3$) layers co-doped with erbium.

were fabricated by electron beam lithography, the Si nanocrystals are partly bleached, most likely reducing the sensitizing efficiency for erbium.

2.8 Conclusions

Silicon nanocrystals are made by magnetron sputtering of silicon in an oxide atmosphere [37]. The nanocrystals can be excited optically, electrically, and by using a high-energy electron beam. Quantum confined emission is observed, peaking at a wavelength of $\lambda = 800$ nm. Luminescence lifetimes range from 10 to 40 µs in the spectral range. By measuring pump up and pump down traces, we found an excitation cross section of $\sigma = 1.9 \times 10^{-16}$ cm^2 at $\lambda = 700$ nm, that increased to $\sigma = 3.5 \times 10^{-16}$ cm^2 for $\lambda = 900$ nm. Electroluminescence is observed, peaking at 675 nm for electrical bias in the range of 15 to 30 V.

By cathodoluminescence experiments we have shown that luminescence of Si nanocrystals bleach under electron beam irradiation to an $1/e$-value for an

electron deposited energy of 0.5 $\mu J/cm^3$, or an electron dose of 150 to 400 $\mu C/cm^2$. Electron beam lithography requires a similar dose [60]. Because of the bleaching, this fabrication technique is unsuited to fabricate nano- and micro-scale structures that include Si nanocrystals.

Samples co-doped with erbium show electroluminescence at $\lambda = 1540$ nm.

Chapter 3

Planar electrical IMI plasmon source

We describe the interaction of Si quantum dots with a gold film that supports surface plasmon polaritons. A device design is presented that incorporates Si quantum dots with a plasmon waveguide geometry. The Si quantum dots are electrically excited and quench by the generation of surface plasmons.

3.1 Introduction

A surface plasmon polariton (SPP) is an electromagnetic wave propagating at the interface between a metal and a dielectric that is coupled to a charge density oscillation by free electrons at the surface of the metal [1, 2]. The intensity of SPPs is concentrated at the interface and the electromagnetic field decays exponentially perpendicular to the interface. Because of absorption at optical frequencies in the metal, SPPs have a finite propagation length that ranges from a few nanometers to several tens of micrometers [1, 2]. SPPs are characterized by their frequency ω and a complex k-vector:

$$k_{\parallel} = k'_{\parallel} + ik''_{\parallel} = \left[\frac{\omega}{c}\sqrt{\frac{\epsilon'_m\epsilon_d}{\epsilon'_m+\epsilon_d}}\right] + i\left[\frac{\omega}{c}\left(\frac{\epsilon'_m\epsilon_d}{\epsilon'_m+\epsilon_d}\right)^{3/2}\frac{\epsilon''_m}{2(\epsilon'_m)^2}\right] \quad (3.1)$$

$$k^2_{\perp m,d} = \epsilon_{m,d}\left(\frac{\omega}{c}\right)^2 - k^2_{\parallel}, \quad (3.2)$$

where $\epsilon_{m,d}$ are the dielectric constants of the metal (m) and dielectric (d) at frequency ω. A dispersion relation for SPPs was already shown in figure 1.1. Since $k_{\perp}$ is purely imaginary, the SPP is an evanescent wave. The propagation length for SPPs is given by $L_{\text{prop.}} = 1/(2k''_{\parallel})$.

Here we propose a structure in which SPPs can be generated electrically in a two-step process: first Si nanocrystals are electrically excited and secondly, the excited nanocrystals couple to a nearby metal/dielectric interface and generate SPPs [16–18, 63]. Figure 3.1 shows a device schematic. On top of a silicon on insulator (SOI) substrate, a layer of SiO_2 with Si nanocrystals is deposited. A gold layer on top provides an electrical contact and supplies a metal/dielectric interface to support SPPs. The nanocrystals are electrically excited (figure 3.1:a); the excited nanocrystals decay by the generation of SPPs (b), the SPP propagates (c), and eventually the SPP is radiated into the far-field by an outcoupling structure (d). We also used erbium co-doped layers to study SPP generation at $\lambda = 1.5$ µm.

3.2 Fabrication

On top of an SOI substrate, a 150 nm thick layer of silicon-rich-oxide (SiO_x, with $x = 1.3$) was deposited, as is described in section 2.2. This layer was then annealed at 1000 °C in an argon atmosphere to form Si nanocrystals and was passivated at 800 °C in a forming gas atmosphere. Because of the high temperatures, the choice of material for the bottom electrical contact is

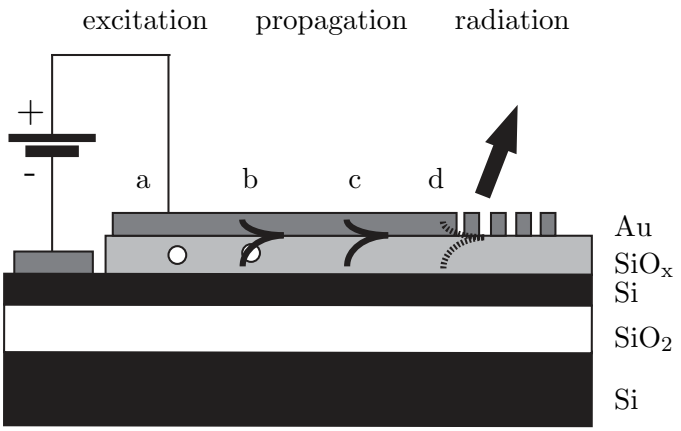

Figure 3.1: Sample structure for the IMI planar plasmon polariton source based on Si nanocrystals. The Si nanocrystals inside the SiO_x layer are electrically excited (a). The excited nanocrystals couple to the metal interface and decay by the generation of surface plasmon polaritons (b). The plasmon propagates for some distance (c) before it is radiated into the far-field by an outcoupling structure (d). For clarity, the cartoon is not to scale.

limited. To solve this problem, we used a highly doped Si device layer of an SOI substrate. To limit the optical absorption of SPPs by the silicon layer, we used a thin device layer of 50 nm, that was separated by a thick (5 µm) buried oxide layer from the carrier wafer. Chapter 5 addresses the problem of the bottom contact in a different way by using low-temperature processes and by fabricating membrane structures.

To use the 1.5 µm wavelength range, a variation to the geometry in figure 3.1 was made by incorporating erbium ions into the SiO_x layer. For this geometry, an additional doped Si layer was added between the SiO_x and the metal top contact to enhance the electrical conductivity (see section 2.7). It is not possible to use this additional Si layer for the SPP source based solely on Si nanocrystals operating in the $\lambda = 600$–900 nm spectral range, because of the absorption of Si.

For both sample designs, electrical contacts to the SiO_x layer and the Si device layer were made by using electron beam lithography, physical vapor deposition of 50 nm of gold, and lift-off, as is explained in section 2.5. The role of the contact on the SiO_x is two-fold: it is an electrical contact and it provides a metal interface to support SPPs. The contact was structured

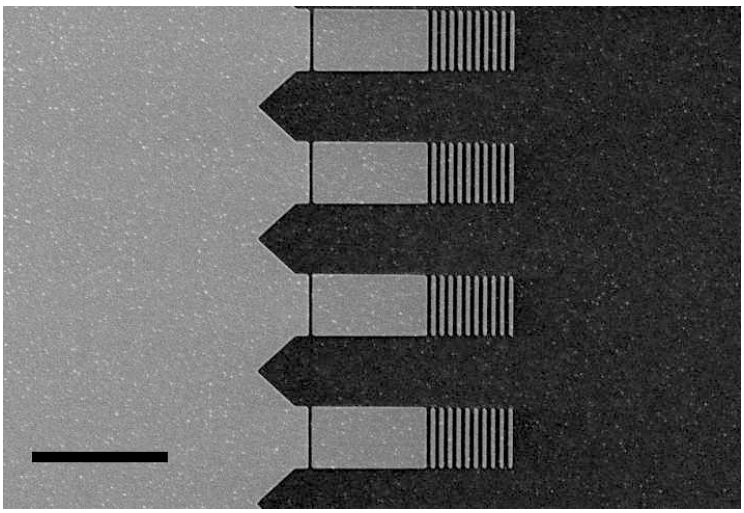

Figure 3.2: SEM image of the device structure. A plasmon waveguide that ends in a grating structure is fabricated by electron beam lithography and lift-off. The light gray area represents the Au area. At the entrance of the waveguide, a small slit separates the waveguide from the electrical contact pad on the left. In this way electroluminescence and reradiated SPPs can be spatially separated. The scale bar is 10 µm.

as is shown in figure 3.2. Plasmon waveguides are connected to the electrical excitation pad. At the beginning of the waveguide, a small slit in the gold layer electrically isolates the waveguide from the excitation pad. SPPs can cross this small slit [64, 65], but because of the electrical isolation, electroluminescence and generation of SPPs underneath the waveguide is not possible. At the end of the waveguide, a grating is used to reradiate SPPs into the far-field for detection. By changing the distance from isolation slit to the outcouple grating, it is possible to measure the propagation length of the SPPs.

3.3 Theory

To calculate the coupling between the Si nanocrystals and SPPs, a model by Ford and Weber was used [66]. The Si nanocrystals were modeled as randomly oriented dipoles, emitting at a single wavelength. Using the model, it is possible to calculate the decay rates based on the optical density of states of a dipole in a layered structure. The model is one dimensional and assumes the structure extends infinitely in the other two dimensions [15]. The emission

from a dipole is expanded into plane waves and the Fresnel-reflection coefficients [55] for each plane wave of the layered structure are calculated. All the reflected waves are summed to find the net reflected intensity at the position of the dipole, from which the power dissipation by the dipole and the decay rate can be calculated. The modification of decay rates by a layered structure was already experimentally shown by Drexhage in the 1960s [67].

The calculated total decay rate can be divided into three parts: a decay path for spontaneous emission, a decay path into SPPs, and a decay path for lossy surface waves. The latter is considered to be due to quenching to the metal [19]. The three decay paths are characterized by the accompanying k-vector. The k-vector can be split into a perpendicular ($k_\perp$) and into a parallel ($k_\parallel$) vector, with their direction relative to the interfaces of the layered structure. Figure 3.3 shows the power dissipation for $k_\parallel$ for a dipole in SiO_2 near a gold/silica interface for three distances to the interface (10, 100, and 1000 nm). For the range of $k_\parallel/k_0$ from 0 to 1 (k_0: the k-vector of a plane wave inside the medium surrounding the dipole), the decay is into spontaneous emission. The range for decay into SPPs is taken $1 < k_\parallel/k_0 < 2k_{\mathrm{SPP}} - 1 = 1.133$, where k_{SPP} is the SPP wave vector ($2\pi/\lambda_{\mathrm{SPP}}$) [68]. Decay into larger k-vectors is due to quenching to the metal [19]. Clearly, for small distances a large degree of quenching occurs, while for large distances spontaneous emission dominates.

Figure 3.4 shows the calculated total decay rate (solid line) for a randomly oriented dipole ($\lambda = 750$ nm) placed in SiO_2 as a function of distance from the interface with a semi-infinite gold layer. Contributions are shown of: spontaneous emission (dashed line), surface plasmon excitation (dotted line) and quenching (small dotted line). The total decay rate shows oscillations with a period of half the wavelength that die out for larger distances. The excitation of SPPs is based on the mode-overlap of the dipole with the SPP and therefore the excitation rate decreases exponentially with increasing distance. The decay to lossy surface waves has a distance dependence between d^{-3} and d^{-4}. If the emitter is close to the metal interface, the dipole can excite electron-hole pairs in the metal. These electron-hole pairs are lost as heat in the metal, because of the scattering of electrons [19]. The creation of electron-hole pairs in the metal can be seen as the excitation of a dipole. The energy transfer between two dipoles has a d^{-6} dependence [69]. Integrating over a sheet of dipoles eventually leads to a d^{-3} dependence. The d^{-4} dependence arises from the creation of an exciton at the surface [19]. The optimum position to excite SPPs is close to the metal (closer than ∼half the emission wavelength), but far enough to not to be hampered by quenching (farther than 20 nm) [19, 70].

Next, we evaluate the coupling of Si nanocrystals to a gold layer with a

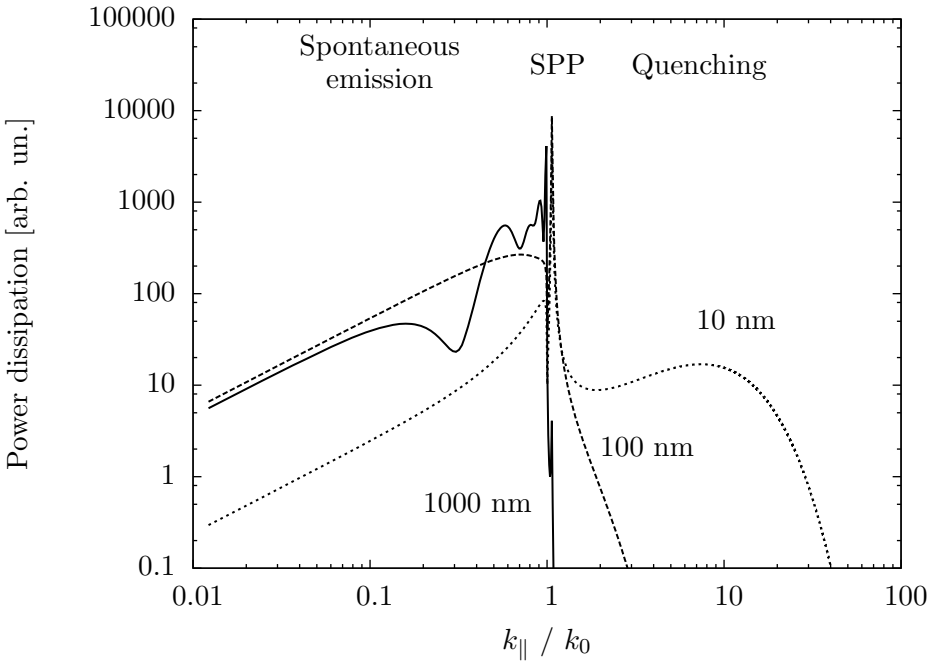

Figure 3.3: Power dissipation of a randomly oriented dipole (λ = 750 nm) in SiO_2 near a Au interface as a function of $k_{\|}$ at different positions from the Au / SiO_2 interface. $k_{\|}$ is normalized to the plane wave vector k_0 in SiO_2. The data up to $k_{\|} = 1$ corresponds to spontaneous emission, data in the range $1 < k_{\|} < 1.133$ represents SPP excitation, and larger k-vectors correspond to quenching to the metal.

thickness smaller than the SPP skin depth in the metal. A thin Au layer is positioned between SiO_2 and air. Both interfaces of the metal support SPPs and these SPP-modes couple to form a symmetric and an antisymmetric mode. The antisymmetric mode has a longer propagation length than the symmetric mode because of its larger mode overlap with the metal [71].

Figure 3.5 shows the decay rate into $k_{\|}$ of a random oriented dipole (λ = 750 nm) at 100 nm distance from the Au/SiO_2 interface for several gold layer thicknesses. The inset shows a sketch of the geometry. The peak for $k_{\|}$ / $k_0 > 1$ corresponds to the symmetric SPP mode. As can be seen, the SPP wave vector is strongly dependent on the Au layer thickness. For thicker gold layers, there are separate SPP modes on the air side and on the SiO_2 side. The SPP at the air side of the gold is leaky into the SiO_2. Besides the SPP

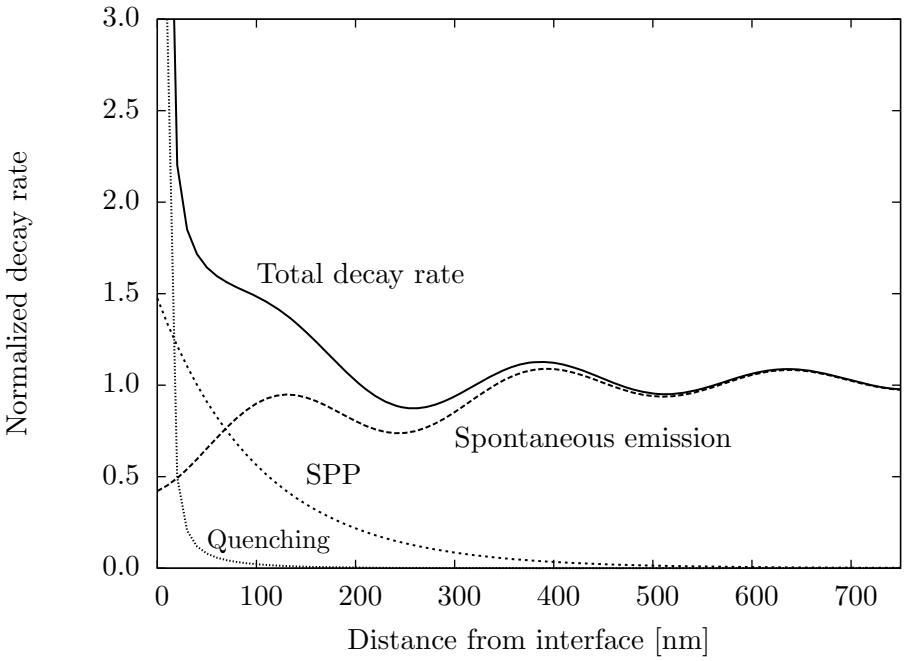

Figure 3.4: Normalized decay rates for a randomly oriented dipole in the SiO_2 layer near the Au/SiO_2 interface emitting at a free space wavelength of $\lambda = 750$ nm in the SiO_2 layer, split into the three components: spontaneous emission, excitation of surface plasmons, and quenching to the metal layer, as a function of the distance of the dipole from the Au/SiO_2 interface. Data are normalized to the spontaneous emission rate in bulk SiO_2.

on the SiO_2 side, there are no other optical modes that exist in the sample geometry of figure 3.2 that can be excited by the nanocrystals.

3.4 Experiments

Experiments were carried out on the sample as is illustrated in figure 3.1. The gold contacts on the Si device layer and the SiO_x were 50 nm thick. With a 488 nm pump laser chopped with an AOM, Si nanocrystals were excited and the photoluminescence decay traces were measured. As reference, a decay trace for Si nanocrystals in SiO_2 on the same sample not covered with Au was also measured. Figure 3.6 shows both decay traces, together with a stretched

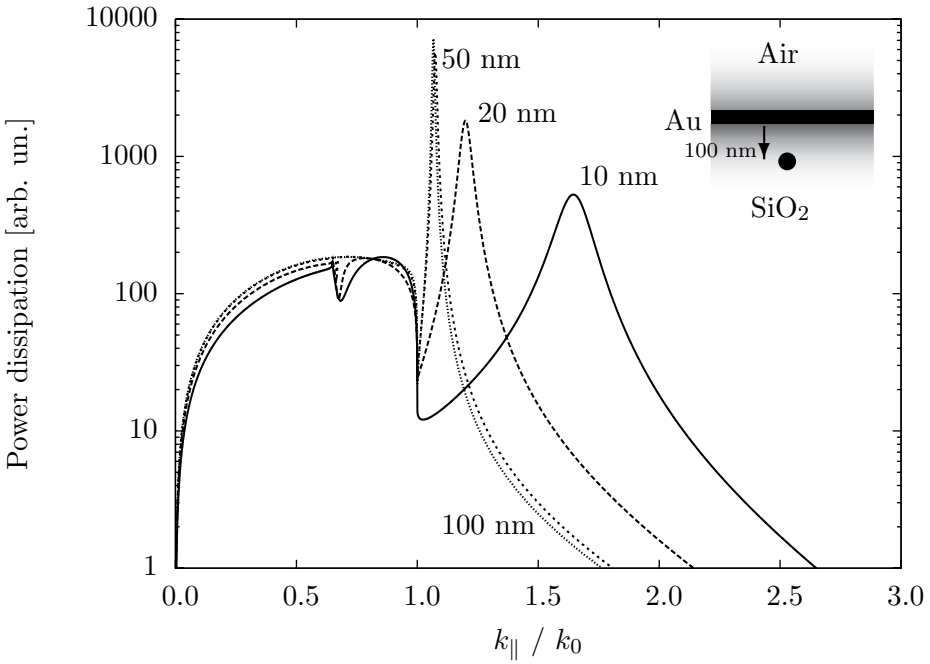

Figure 3.5: Power dissipation of a randomly oriented dipole ($\lambda = 750$ nm) into $k_\parallel$ at 100 nm distance from the SiO_2/Au interface (see inset) for several gold layer thicknesses. The dielectric material on the other side of the gold is air. A symmetric SPP mode exist with $k_\parallel$ larger than 1. The SPP mode on the air side of the gold is leaky into the SiO_2. For thicker gold layers, the two modes decouple and separate into SPPs on both sides of the gold.

exponential fit to the data. The decay of the nanocrystals underneath the gold layer was faster ($\tau = 24$ µs, $\langle\tau\rangle = 85$ µs) than the decay of the reference nanocrystals ($\tau = 38$ µs, $\langle\tau\rangle = 94$ µs). This is in qualitative agreement with figure 3.4. Both the excitation of SPPs and quenching to the gold will raise the decay rate. The emission quantum efficiency of the nanocrystals can be estimated by using the method of references [47, 72]. The calculated optical density of states for the nanocrystals covered by the gold layer is 1.5 times the calculated density of states for the nanocrystals used as reference. From this calculation and the ratio in measured average lifetimes $\langle\tau\rangle$, we calculate a quantum efficiency for the emission of Si nanocrystals of 20%, which is on the same order as found in literature [47].

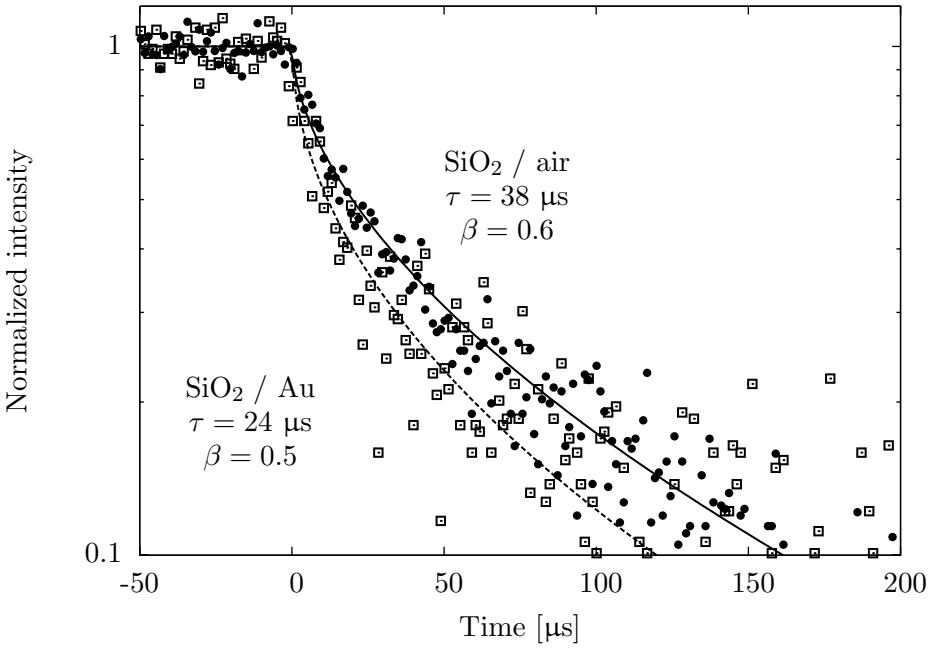

Figure 3.6: Normalized photoluminescence decay traces at $\lambda = 900$ nm for Si nanocrystals in SiO_2 with and without a gold layer. The presence of gold increases the decay rate of the nanocrystals due to coupling to SPPs.

The sample was mounted onto a printed circuit board, and was electrically contacted by wire bonding. The sample showed clear electroluminescence, but instead of obtaining a homogenous distribution of electroluminescence and SPP-generation, a random collection of hotspots was observed in optical microscopy. The hotspots were quite intense, as the luminescence could be observed by the naked eye in a darkened room. Unfortunately, the current through the hotspots deteriorated the gold contact and eventually removed gold from the SiO_x layer (see figure 2.6).

In one of the structures, a single hotspot was located close to the beginning of a plasmon waveguide. With an inverted scanning confocal optical microscope line scans of light emission at positions along the waveguide were measured. A polarizer was inserted into the parallel optical beam path of the microscope. Two line scans were measured using the polarizer in longitudinal direction (the polarization expected for propagating SPPs) and in transverse direction as reference. The confocal microscope was connected to a

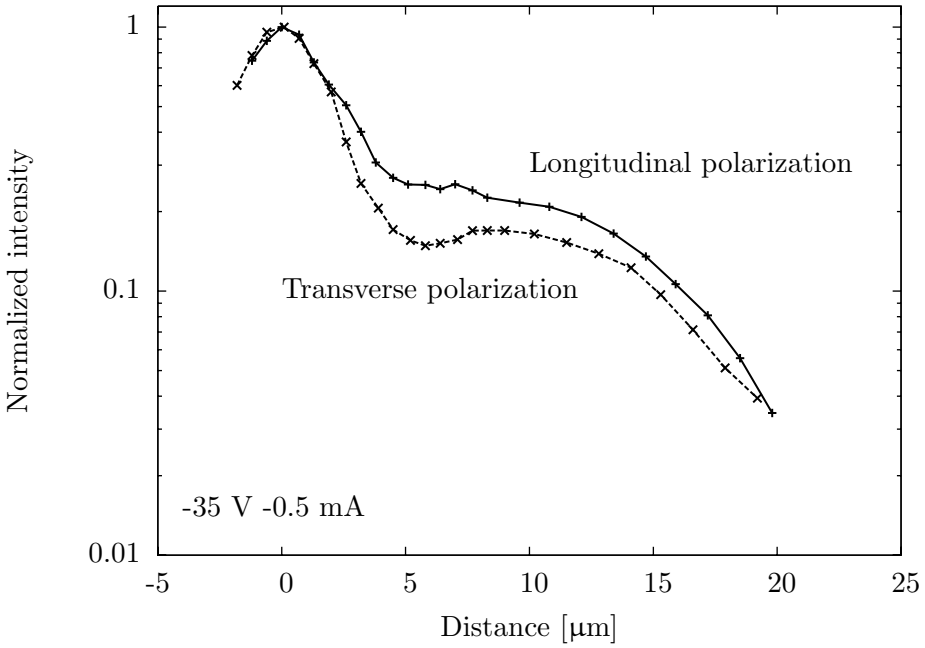

Figure 3.7: Line scans at $\lambda = 650$ nm to detect electroluminescence and outcoupled surface plasmons, taken using a scanning confocal microscope. Emission with longitudinal polarization shows a higher intensity, which is expected for surface plasmons.

spectrometer in order to obtain spatially, spectrally, and polarization resolved information with a single measurement.

Figure 3.7 shows a line scan over the waveguide for both polarizations at a free space wavelength of $\lambda = 650$ nm. The location of the hotspot is defined as the zero-position and the intensities are normalized. The first drop in intensity (up to 5 μm) is due to the convolution of the detection spot size of 3 μm with the size of the hotspot. For distances larger than 5 μm, the longitudinal polarization intensity decays slower than the transverse polarization.

Line scans as shown in figure 3.7 were measured for the entire luminescence spectrum of the Si nanocrystals. Figure 3.8 shows the longitudinally polarized line scans for several wavelengths. For all of these traces, the transverse polarized line scans have lower intensity, similar as in figure 3.7 (not shown). For longer wavelengths, the apparent propagation distance increases, which is in qualitative agreement with what is expected for SPPs.

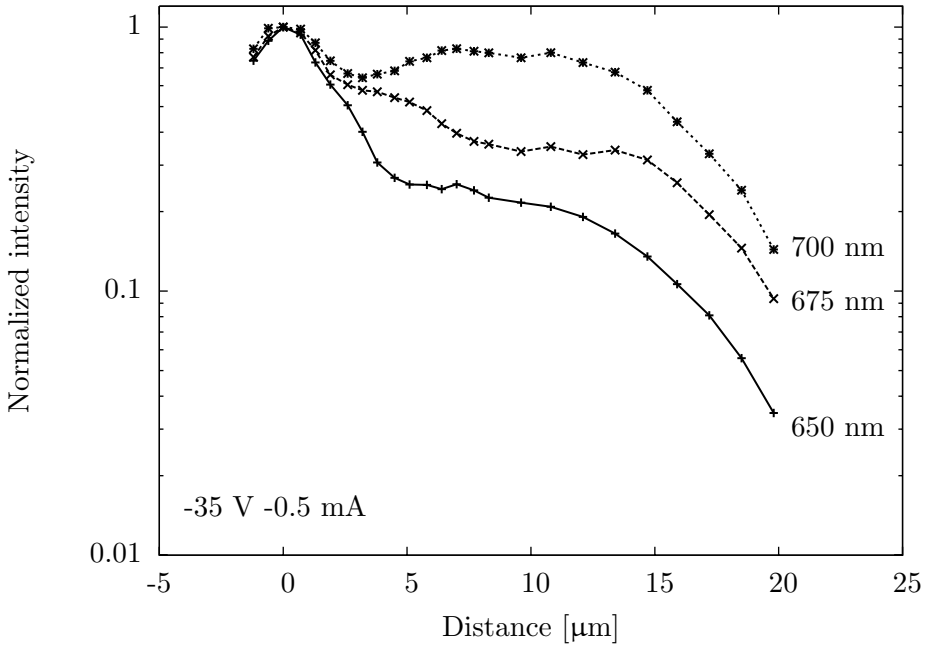

Figure 3.8: Line scans to detect longitudinally polarized electroluminescence and outcoupled surface plasmons, made by a scanning confocal microscope. Surface plasmons with a larger wavelength have a longer propagation length, as expected.

To fabricate an SPP source at $\lambda = 1.5$ μm, the SiO_x layer was doped with erbium (see section 2.7 on the electroluminescence of erbium). A sample was fabricated as is described in section 2.2. On top of the SiO_x layer (150 nm, with $x = 1.3$), an additional 50 nm thick Si layer was deposited to improve on the electrical conduction of the device. The SiO_x was then implanted with erbium and the top Si layer is implanted with boron. The maximum concentration of Er (1 at.%) is positioned at the center of the SiO_x-layer. After an anneal step at 900 °C, the sample was mounted onto a printed circuit board and electrical contacts were made by wire bonding. Similar experiments were performed as described above.

Figure 3.9 shows a line trace of emission at $\lambda = 1.5$ μm along the waveguide. An infrared sensitive InGaAs photodiode-array coupled to a spectrometer was used as a detector. Each point on the graph is a result of the average of 30 separate background-corrected measurements on the same location of the

sample. The error bars reflect the standard deviation of the mean of the measured intensities. The line connecting the points is a guide to the eye. The inset on the top part of the figure shows the approximate position of the waveguide itself. At two positions along the waveguide (at 0 μm and around 8 μm) an increase of emitted light is observed. These two positions coincide with the electrical isolation slit (at 0 μm) and with the grating (at 8 μm). The light collected from the isolation slit could be resulting from electroluminescence that is excited in the pad next to it. Light collected from the outcoupling grating is assigned to radiation due to waveguide modes at the structure. These could be SPPs propagating over the Au waveguide; or due to an optical TE waveguide mode, excited under the electrical pad. In the next chapter, a novel design is introduced in which the TE mode does not exist.

3.5 Conclusions

We have studied the coupling between electrically excited Si nanocrystals as well as Er ions to surface plasmons on gold. A device design is introduced that is composed of a source, waveguide, and outcoupling gratings. We calculate the coupling between the nanocrystals and SPPs, by a model by Ford and Weber. To excite SPPs efficiently, the best position for an emitter is at a distance between 20 and 300 nm from the SiO_2 / Au interface.

Electroluminescence of Si nanocrystals was obtained from the fabricated samples, yet the luminescence appeared as hotspots instead of a homogeneously distributed luminescence. One of the hotspots was located at the entrance of a waveguide. Line scans made with a scanning confocal optical microscope show that the longitudinal polarization has a higher intensity than the transverse polarization, in agreement with the expectation for SPPs. For longer wavelengths, the detected intensity along the line scans decays slower, which can be explained by the longer SPP propagation length for these wavelengths. For the Er-doped structure, a clear output signal is measured at the outcoupling grating, that can be assigned to surface plasmons as well as a photonic waveguide mode.

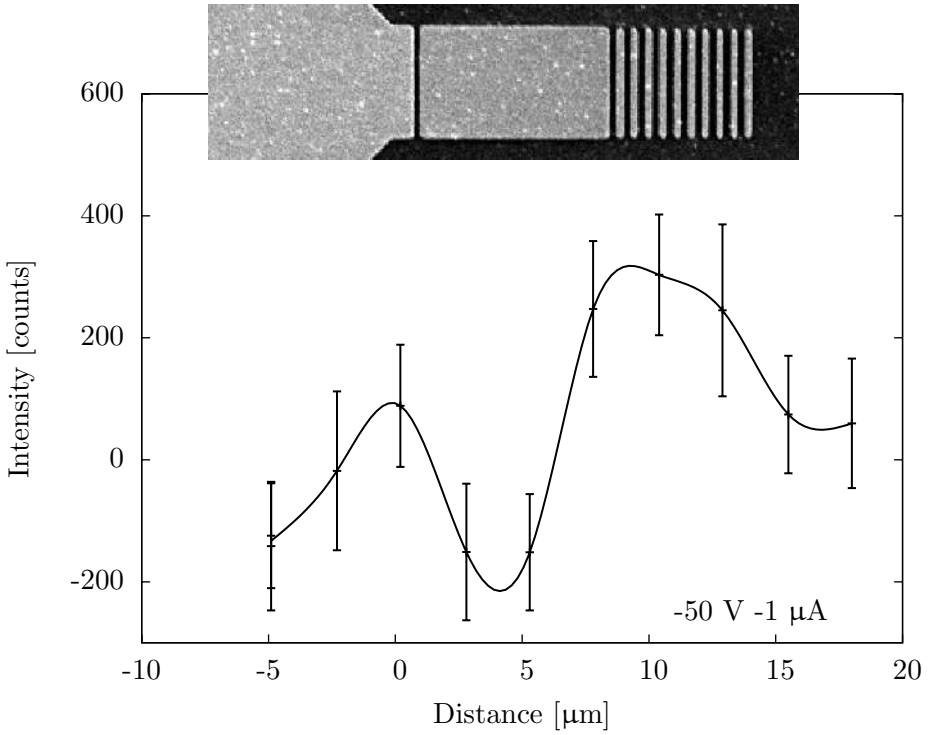

Figure 3.9: Confocal line scan along a surface plasmon waveguide to detect electroluminescence and outcoupled surface plasmons with a free space wavelength of $\lambda = 1540$ nm. The SiO_x layer is implanted with erbium. The line is a guide to the eye. The inset shows an SEM image of the structure roughly aligned with the optical measurement.

Chapter 4

Optical properties of silicon nanocrystals in an alumina matrix

Samples containing nanostructured silicon layers in alumina were prepared by a combination of atomic layer deposition (ALD) and chemical vapor deposition (CVD) techniques at low temperature (325 °C). The as-deposited samples show photoluminescence and electroluminescence properties that are consistent with emission from silicon nanocrystals. Time-resolved measurements and comparison to reference samples containing silicon nanocrystals in silica suggest that non-radiative recombination dominates in the majority of nanocrystals. However, we also observe microsecond-scale photoluminescence decay components suggesting that some nanocrystals emit light with an internal quantum efficiency as high as 1%.

4.1 Introduction

Silicon nanocrystals in alternative host matrices than SiO_2 are of significant fundamental interest because of the suspected importance of interface states in exciton recombination and of dielectric screening in energy transfer processes. The details of silicon nanocrystal formation and morphology could additionally change with the host material. Alternatives to silica are also of technological interest; optical materials that can be realized through low-temperature methods that are compatible with back-end CMOS processing may find wider application.

We characterize the luminescence properties of silicon nanocrystals in an alumina (Al_2O_3) host matrix prepared by low-temperature methods that are back-end CMOS compatible [35]. This material exhibits near-infrared and visible photoluminescence (PL) and electroluminescence (EL) as deposited.

4.2 Fabrication

Silicon nanocrystals in an alumina matrix were deposited by a combination of atomic layer deposition (ALD) and low pressure chemical vapor deposition (LPCDV) onto a silicon substrate, as will be described next. This work was performed in the group of Prof. Dr. J. Schmitz at the University of Twente. The Si substrate (100) was cleaned and the native oxide was etched by a 0.3% HF and 0.3% HCl solution, after which the wafer was immediately loaded into the vacuum system. First a monolayer of trimethylaluminium was deposited onto the substrate and then, after purging the deposition chamber with nitrogen, the substrate was exposed to water to form alumina. The thickness of this deposited Al_2O_3 layer is 0.08 nm. This cycle was repeated 125 times to obtain a layer thickness of 10 nm. Without breaking the vacuum, the wafer was transferred to a low-pressure chemical vapor deposition (LPCVD) reactor, where Si was deposited onto the sample by using Si_3H_8 as precursor gas. As will be discussed further, the size of the Si nanocrystals can be tuned by changing the deposition time of Si. After the Si deposition, the wafer was transferred to the ALD reactor, again without breaking the vacuum. A layer of 10 nm Al_2O_3 was deposited by the same ALD process to encapsulate the Si nanocrystals. In contrast to earlier work [73, 74], the entire deposition process was performed at low temperatures ($T < 325$ °C), which satisfies the requirements for back-end CMOS processing. More information about the deposition process can be found in reference [35].

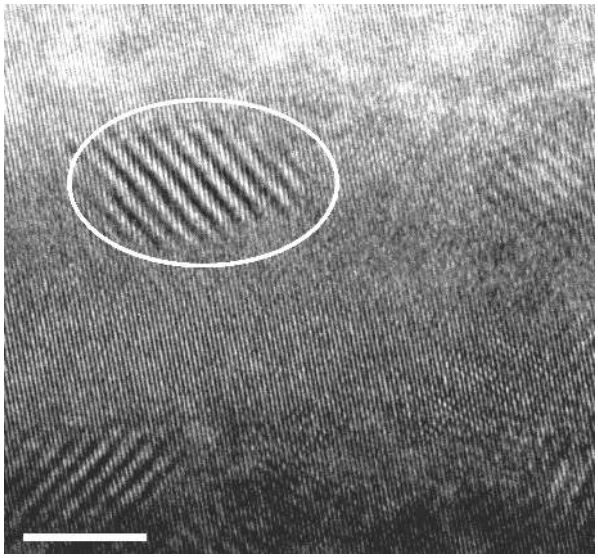

Figure 4.1: Plan view TEM image of Si nanocrystals in alumina. A single nanocrystal is enclosed with the white contour. The parallel lattice planes indicate single-crystallinity. The scale bar is 5 nm.

Figure 4.1 shows a plan-view transmission electron microscope (TEM) image of the as-deposited sample, without the top Al_2O_3 layer. The Si deposition time was 10 minutes in a pressure of 10 mbar. The image shows crystalline features, which are attributed to Si nanocrystals. The size of the nanocrystals is in the range of 5–8 nm. An SEM image of a cross section of the alumina layer with Si nanocrystals is shown in figure 5.8 (chapter 5).

4.3 Photoluminescence

Photoluminescence spectra were measured by the same method as explained in section 2.4. The nanocrystals were excited by using the 488 nm line of an argon-ion laser. The luminescence was collected by a $f = 2.5$ cm (NA = 0.45) lens and sent to a spectrometer. A low-pass filter separates the excitation laser from the luminescence signal.

Figure 4.2 shows normalized photoluminescence (PL) spectra for as deposited samples. The spectra show a clear peak at $\lambda = 800$–900 nm. The Si deposition time for the five samples was increased from 5 minutes to 10, 20, 30, and 60 minutes with a pressure of 1 mbar for all samples. The samples with a

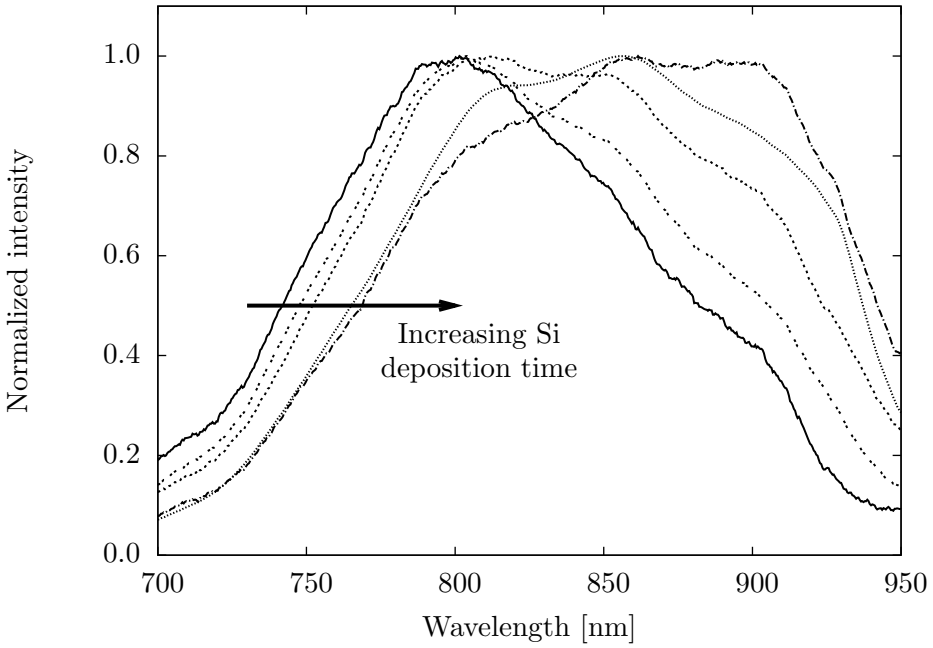

Figure 4.2: Normalized photoluminescence spectra of Si nanocrystals in Al_2O_3. The Si deposition times increases from 5 minutes to 10, 20, 30, and 60 minutes, resulting in larger Si nanocrystals and thus redshifted luminescence. The pump wavelength was 488 nm.

deposition time of 30 and 60 minutes consist of a multilayer of four layers of Si nanocrystals with Al_2O_3 layers in between. The other samples consist of only a single layer of Si nanocrystals encapsulated with Al_2O_3 on both sides. A longer deposition time results in larger nanocrystals and therefore a redshift in the spectrum is expected. Figure 4.2 indeed shows a redshift of the PL spectrum for longer Si deposition times.

The excitation laser was switched on/off by using an AOM and the time-resolved luminescence was measured with a PMT (see section 2.4). A sample with four Si nanocrystal layers (30 minutes Si deposition time) was characterized. Figure 4.3 shows luminescence spectra for several times after switching off the excitation laser ranging from $t = 0$ to 40 µs. The nanocrystal luminescence at the wavelength $\lambda = 850$ nm has a decay rate of 3.4 MHz. The signal observed at $\lambda < 600$ nm is due to defect luminescence, unrelated to nanocrystals and decays within 50 ns (system response time).

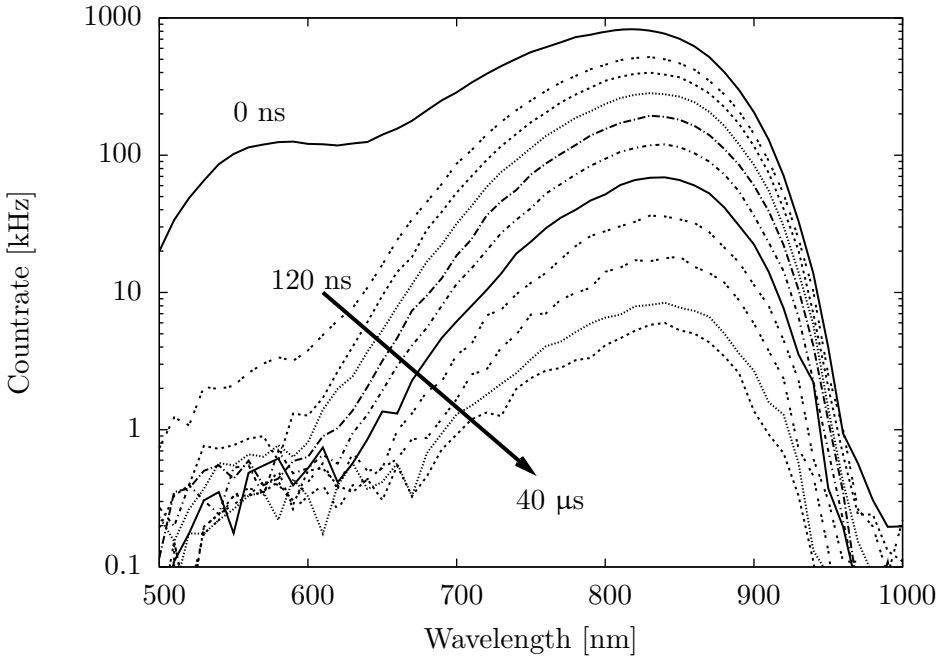

Figure 4.3: Photoluminescence spectra of Si nanocrystals in Al_2O_3 for several times after switching off the excitation laser (λ = 488 nm). The times are: 0, 0.12, 0.2, 0.4, 0.8, 1.6, 3.2, 6.4, 12.8, 25.6, and 40 µs.

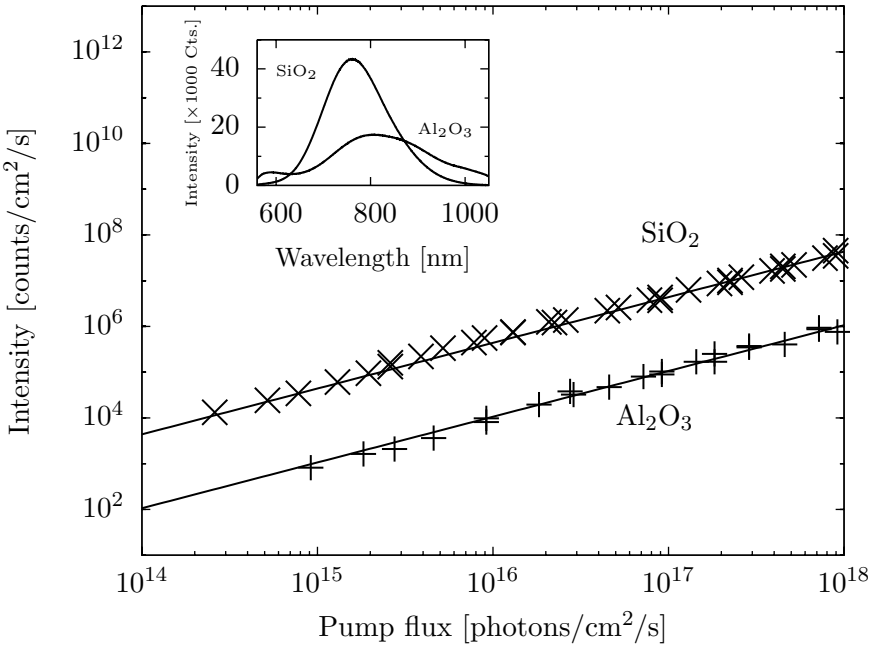

Figure 4.4: Luminescence intensities as a function of excitation photon flux for a reference sample of Si nanocrystals in SiO_2, and for Si nanocrystals in Al_2O_3. The inset shows the PL spectra of both samples.

The peak luminescence intensity is measured as a function of excitation power. Figure 4.4 shows the PL intensity increase for the same sample as in figure 4.3 for an increasing excitation rate (symbol: +). The figure also shows the increase in intensity of a well-characterized reference sample of Si nanocrystals in SiO_2 [75] (symbol: ×). This sample was made by ion-implantation of Si^+ into 15 nm of SiO_2 to an excess Si concentration of 20 at.%, 10 nm from the interface. The nanocrystal areal density is 4×10^{12} cm^{-2}. The inset of figure 4.4 shows the PL spectra of both samples.

The luminescence of Si nanocrystals is modeled by a two-level system. The change in the number of excited nanocrystals (N') is given by:

$$N' = \sigma\phi(N_0 - N) - \Gamma N, \tag{4.1}$$

where σ is the excitation cross section, ϕ is the excitation photon flux, N_0 is the areal density of nanocrystals, N is the areal density of excited nanocrystals and Γ is the observed total decay rate of the nanocrystals. For a steady state

solution, N' equals zero and the number of excited nanocrystals is expressed as:

$$N = \frac{\sigma\phi N_0}{\Gamma + \sigma\phi}. \tag{4.2}$$

In the low pump power regime, where $\sigma\phi \ll \Gamma$, equation 4.2 simplifies to $N = \sigma\phi N_0/\Gamma$. The measured luminescence intensity I is proportional to $\alpha N\Gamma_r$, where Γ_r is the radiative decay rate and α is the detection efficiency:

$$I = \alpha N\Gamma_r = \frac{\alpha\sigma\phi N_0\Gamma_r}{\Gamma + \sigma\phi}. \tag{4.3}$$

Figure 4.4 shows a fit to the data by using equation 4.3, assuming the detection efficiency α was the same for both measurements and the intrinsic radiative decay rate is equal for both samples, but varies because of a different optical density of states. Table 4.1 shows the parameters for the fit. For the SiO_2 reference sample, a value of $\alpha = 1 \pm 0.2 \times 10^{-7}$ counts/NC was obtained. This value was used to fit the excitation cross section σ for Si nanocrystals in Al_2O_3 to $\sigma = 1 \pm 0.3 \times 10^{-15}$ cm^2. The larger cross section compared to SiO_2 may be due to the larger size of nanocrystals in alumina. Indeed, the spectrum in the inset of figure 4.4 shows a redshift in PL for the alumina compared to silica. The assumption for the radiative decay rate to $\Gamma_r = 9.8$ kHz leads to a quantum efficiency (QE) for Si nanocrystals in alumina of 0.3%.

Table 4.1: Material properties and parameters to fit the obtained luminescence intensity data in figure 4.4 for the SiO_2 reference sample and the Al_2O_3 sample.

	Si nanocrystals in SiO_2 [75]	Si nanocrystals in Al_2O_3
	implantation	ALD and LPCVD
$T_{annealing\ /\ deposition}$	1050 °C	325 °C
N_0	4×10^{12} cm^{-2}	2×10^{12} cm^{-2} [35]
α	$1 \pm 0.2 \times 10^{-7}$ cts/NC	1×10^{-7} cts/NC
σ	6×10^{-16} cm^2	$1 \pm 0.3 \times 10^{-15}$ cm^2
Γ	37.7 kHz	3.4 MHz
Γ_r	14 kHz	9.8 kHz
QE	27%	0.3%

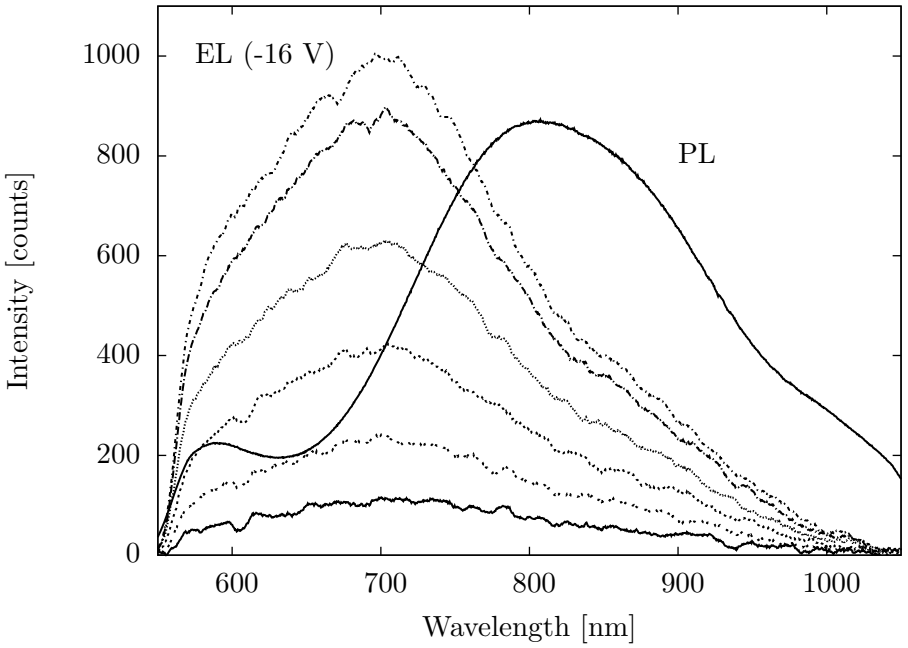

Figure 4.5: Electroluminescence spectra of Si nanocrystals in Al_2O_3 at -12.8, -13.9, -14.8, -15.5 and -16.3 V. The photoluminescence spectrum is shown as reference ($\lambda_{\text{pump}} = 488$ nm).

4.4 Electroluminescence

The rear side of the Si substrate was coated with 100 nm of gold to electrically contact the sample. A semitransparent gold film (10 nm thick) was sputtered onto the alumina (front side) and this gold film was contacted by a probe needle. The sample was biased using a current-source, with the contact on the Al_2O_3 negatively biased with respect to the contact on the Si substrate. Figure 4.5 shows electroluminescence (EL) spectra for several different biassing conditions. As a reference, also a PL spectrum is shown. The EL spectra peak at 700 nm, which is 100 nm blueshifted with respect to the PL spectrum, which we attribute to the difference in excitation mechanism. For higher bias voltages, the EL intensity increases.

The increase in EL intensity for higher biasing conditions in shown in figure 4.6. This figure also shows the current–voltage characteristics. The EL intensity increases linearly with current. The I–V curve shows a clear rectifying

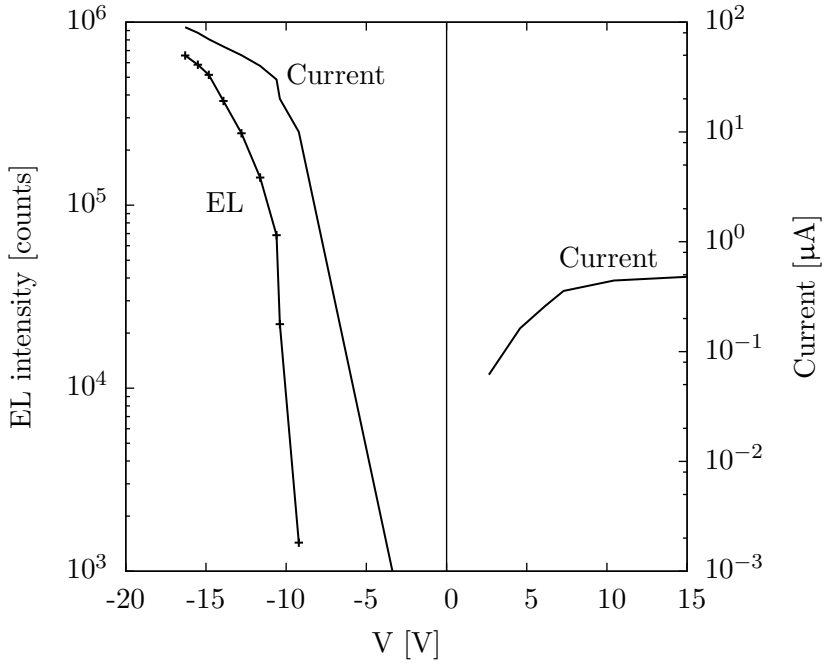

Figure 4.6: Electroluminescence intensity integrated over λ = 500–1000 nm spectral range (left y-axis) and currents through the device (right y-axis) for higher biasing voltages for Al_2O_3 doped with Si nanocrystals.

behavior. No electroluminescence was observed for positive bias conditions.

4.5 Conclusions

Silicon nanocrystals in an alumina host matrix were fabricated at low temperatures (T < 325 °C) by ALD of Al_2O_3 and LPCVD of Si. By regulating the Si deposition time, the size of the nanocrystals can be tuned. Longer deposition times result in larger nanocrystals. The nanocrystals show quantum confined photoluminescence with a peak wavelength of λ = 800 nm and a width of 150 nm FWHM, where the emission spectrum shows a redshift for larger nanocrystals, consistent with quantum confined luminescence. The decay rate is 3.4 MHz (τ = 0.3 μs).

The excitation cross section at λ = 800 nm obtained by a quantitative comparison to a reference sample of Si nanocrystal in SiO_2 [75] is $\sigma = 1 \pm$

0.3×10^{-15} cm^2. We estimate the quantum efficiency to be 0.3%.

Electroluminescence of the Si nanocrystals is observed for negative biasing conditions. The EL spectrum is 100 nm blueshifted with respect to the photoluminescence spectrum. The intensity increases for higher biasing conditions and scales linearly with applied current. The sample shows a clear rectifying behavior with larger currents in negative bias.

The observed electroluminescence, and the low-temperature deposition process (compatible with CMOS back-end processes), makes the presented Si nanocrystal in alumina an interesting material for further technological developments.

Chapter 5

Planar electrical MIM plasmon source

A metal–insulator–metal structure composed of a 600 nm thick gold / alumina / gold membrane geometry is fabricated. The alumina layer is doped with silicon nanocrystals. The nanocrystals are electrically excited by applying a bias across the alumina membrane and decay by generating SPPs. By performing measurements on outcoupling structures in plasmon waveguides integrated with the plasmon source, we demonstrate electrically excited SPPs.

5.1 Introduction

In chapter 3, the electrical excitation of SPP modes on an insulator–metal–insulator (IMI) structure was described. In this chapter, we are considering metal–insulator–metal (MIM) modes, in which an insulator is sandwiched between two metal layers. The surface plasmon modes on either interface couple to form a symmetric and an antisymmetric mode, similar to the IMI-case. We have used gold as metal on both the top and bottom side of our structure and alumina doped with Si nanocrystals as insulator. In the simplest geometry, such an MIM structure would be fabricated by the subsequent deposition of the M, I, and M layers on a substrate. However, the roughness at the interfaces that is introduced will cause significant propagation losses of the MIM plasmons. Here, we introduce a novel design, in which the alumina layer is deposited onto a Si substrate using atomic layer deposition, leading to atomically smooth interfaces. The Si substrate was etched through from the backside, to reveal an alumina membrane spanning across the hole. Au was then deposited on both sides, yielding atomically smooth Au/Al_2O_3 interfaces.

Figure 5.1 shows a schematic of the MIM geometry in cross-section. The MIM structure is the membrane structure in the middle, where there is a hole in the Si substrate. The bottom and the top gold metal contacts were used to bias the active layer with the Si nanocrystals. It was shown in chapter 4 that Si nanocrystals in a similar geometry show electroluminescence. On the bottom side of the membrane, an electrical isolation slit was fabricated similar as in section 3.2. SPPs are generated at the right hand side in figure 5.1. SPPs can cross the isolation slit and are eventually radiated into the far-field by an outcoupling structure that is made on the top side of the membrane. Several outcoupling structures were made, each with different distance to the isolation slit, in order to probe the propagation length of the electrically generated SPPs.

5.2 Theory

The dispersion relation and propagation distance of SPPs can be calculated by applying the appropriate boundary conditions to the Maxwell equations [55] along a metal/dielectric interface and solving the differential equation by using the wave-equation [1]. For the MIM system, there exist modes with symmetric and antisymmetric field distributions. These modes are found by solving the

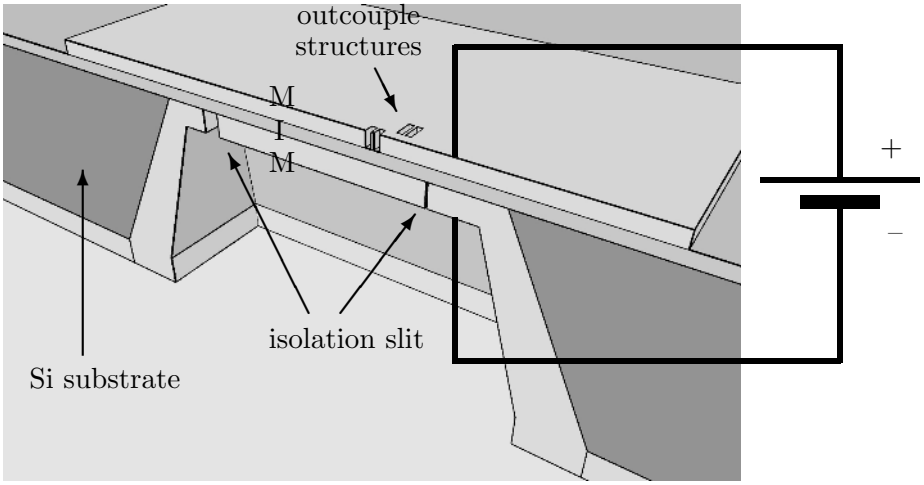

Figure 5.1: Schematic of a crosscut illustrating the MIM plasmon source. An MIM membrane composed of an alumina layer doped with Si nanocrystals embedded between two metal layers spans over a hole in the Si substrate. SPPs are launched by applying a bias across the MIM membrane at the right hand side. The slits on the bottom side provides electrical isolation. Outcoupling structures on the top side of the membrane radiate SPPs into the far-field. The image is not to scale.

equations [9]:

$$\text{symmetric:} \quad \epsilon_d k_{z,m} + \epsilon_m k_{z,d} \tanh\left(\frac{-idk_{z,d}}{2}\right) = 0 \tag{5.1}$$

$$\text{asymmetric:} \quad \epsilon_d k_{z,m} + \epsilon_m k_{z,d} \coth\left(\frac{-idk_{z,d}}{2}\right) = 0, \tag{5.2}$$

in which d represents the thickness of the insulator and $\epsilon_{\mathrm{d,m}}$ are the dielectric constants of the dielectric material (d) and the metal (m) respectively. k_z is the k vector component perpendicular to the layer structure and is related to k_x and the frequency ω by:

$$k^2_{z,(d,m)} = \epsilon_{(d,m)} \left(\frac{\omega}{c}\right)^2 - k_x^2, \tag{5.3}$$

with x the propagation direction.

The SPP mode decays exponentially perpendicular to the interface inside the metallic cladding layers. Inside the insulator the $\mathrm{H_y}$ field profile is either

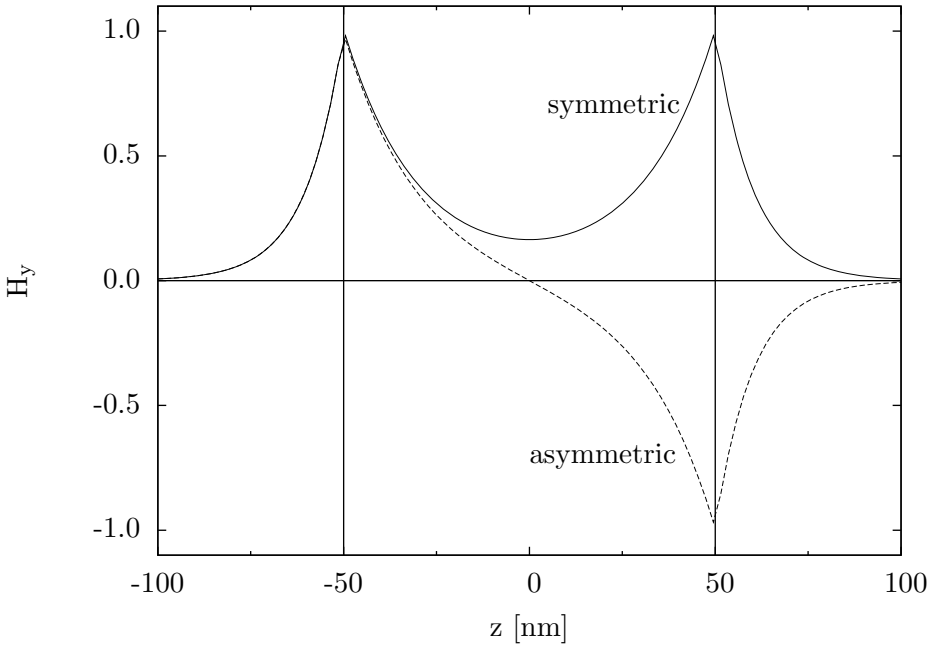

Figure 5.2: Normalized H_y field for symmetric and asymmetric MIM SPP modes. The insulator thickness is 100 nm. The perpendicular k vector components are $k_{z,d} = 0.05$ nm^{-1} and $k_{z,m} = 0.1$ nm^{-1}.

symmetric or asymmetric with respect to the center of the structure. The symmetric mode profile is given by [9]:

$$-d/2 < z < d/2: \quad H_y = e^{-k_{z,d}z} - e^{k_{z,d}z} \tag{5.4}$$

$$|z| > d/2: \quad H_y = (e^{-k_{z,d}d/2} - e^{k_{z,d}d/2})e^{ik_{z,m}(z-d/2)}, \tag{5.5}$$

and for the asymmetric mode profile [9]:

$$-d/2 < z < d/2: \quad H_y = e^{-k_{z,d}z} + e^{k_{z,d}z} \tag{5.6}$$

$$|z| > d/2: \quad H_y = (e^{-k_{z,d}d/2} + e^{k_{z,d}d/2})e^{ik_{z,m}(z-d/2)}. \tag{5.7}$$

In these formulas, z is the position in the MIM geometry measured from the center of the structure and the other symbols are as mentioned above. Figure 5.2 shows the mode profiles of both modes for an insulator thickness of $d = 100$ nm. The asymmetric mode profile has zero intensity at the center; the symmetric mode does not go to zero at the center of the structure.

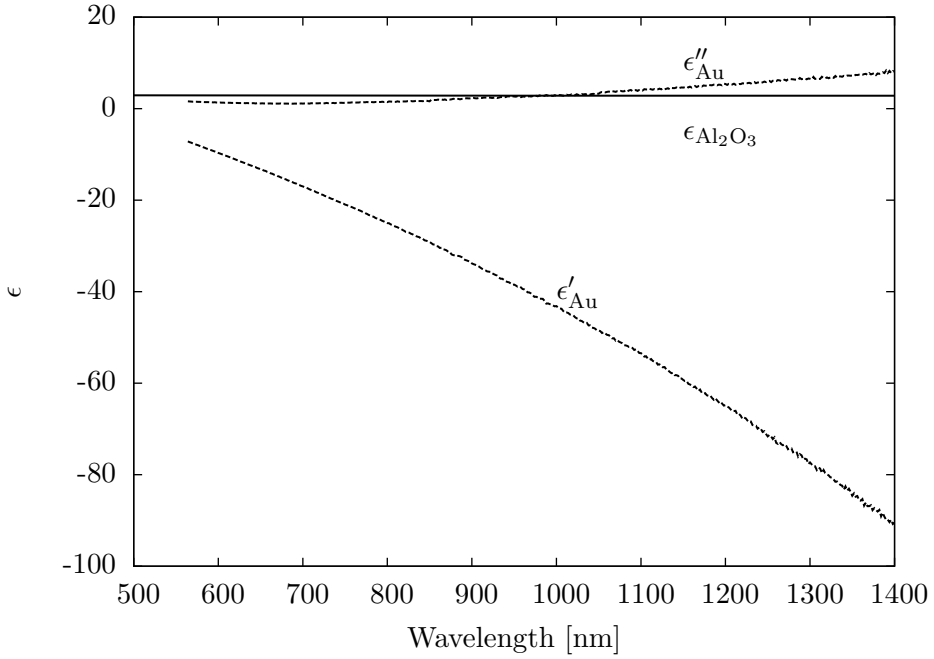

Figure 5.3: Measured values of the dielectric constants of deposited gold ($\epsilon_{Au} = \epsilon'_{Au} + i\epsilon''_{Au}$) and alumina ($\epsilon_{Al_2O_3}$). The alumina has very little dispersion and the dielectric constant is almost constant, $\epsilon_{Al_2O_3} = 2.9$ over the entire measurement range.

For a given frequency, the complex wave vector k_x is obtained by solving equations 5.1 and 5.2 numerically by using a variation of the Powell hybrid method. As input parameters for the dielectric constants, we have used the results of spectral ellipsometry of both the alumina and the gold. The measured dielectric constants of both materials are shown in figure 5.3. Alumina has very little dispersion in the entire measurement range and is almost constant at $\epsilon_{Al_2O_3} = 2.9$. For gold, both the real part (ϵ'_{Au}) and the imaginary part (ϵ''_{Au}) are plotted.

Figure 5.4 shows the obtained dispersion relation for the symmetric MIM SPP. Also the dispersion relation for the planar plasmon at a semi-infinite gold/alumina interface and the light line in alumina are plotted. As can be seen, for thinner dielectric layers, the dispersion relation shifts to larger k-vectors, i.e. smaller wavelengths are obtained. For a photon energy of 2.2 eV ($\lambda = 564$ nm) for the 50 nm thick Al_2O_3 layer, a two-fold reduction in wave-

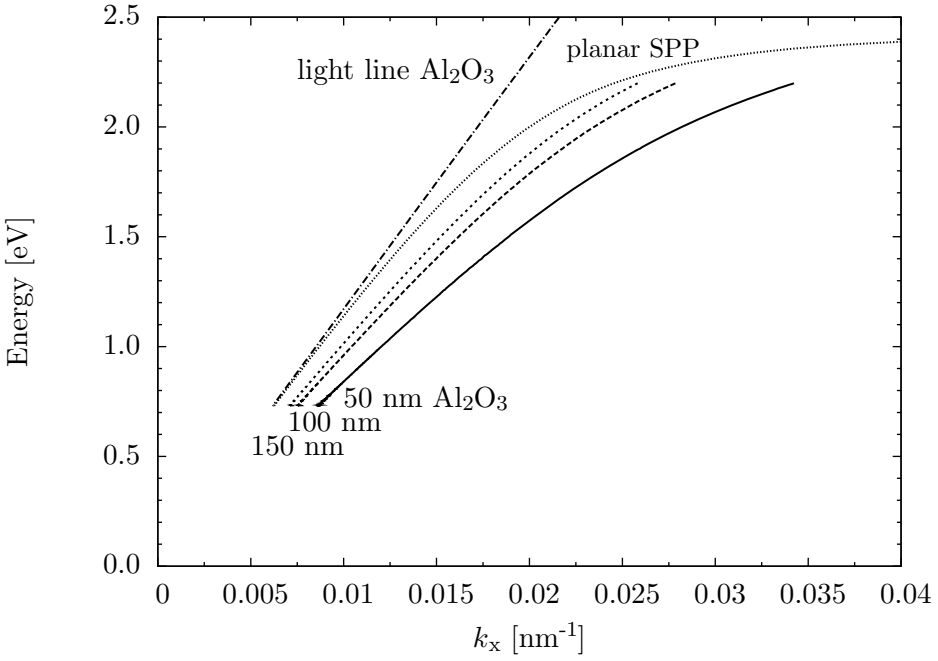

Figure 5.4: Dispersion relation calculated for a planar Au/Al_2O_3 surface plasmon mode (dotted line) and for symmetric MIM $Au/Al_2O_3/Au$ surface plasmon mode (Al_2O_3 thicknesses: 50, 100, and 150 nm), based on measured dielectric constants. The dashed line shows the light line in Al_2O_3.

length is found compared to the wavelength in Al_2O_3.

The imaginary part of the plasmon wave vector k determines the propagation length of the plasmon; $L_{prop} = 1/(2k'')$ (see section 3.1). The propagation distance for the symmetric MIM mode for the three layer thicknesses is plotted in figure 5.5, again based on measured values of the dielectric constant. For thinner dielectric layers, the plasmon gets more confined and the propagation length shortens, due to a larger field concentration in the metal. Also the propagation length for SPPs at a single Au/Al_2O_3 interface is plotted. Note that the MIM waveguide supports an asymmetric plasmon mode (see figure 5.2); this mode has extremely small propagation length and is therefor not considered further. The dispersion relation in similar MIM systems has been studied experimentally [76, 77] and was in good agreement with calculations.

In the experiment, we have chosen to use an insulator thickness of 100 nm.

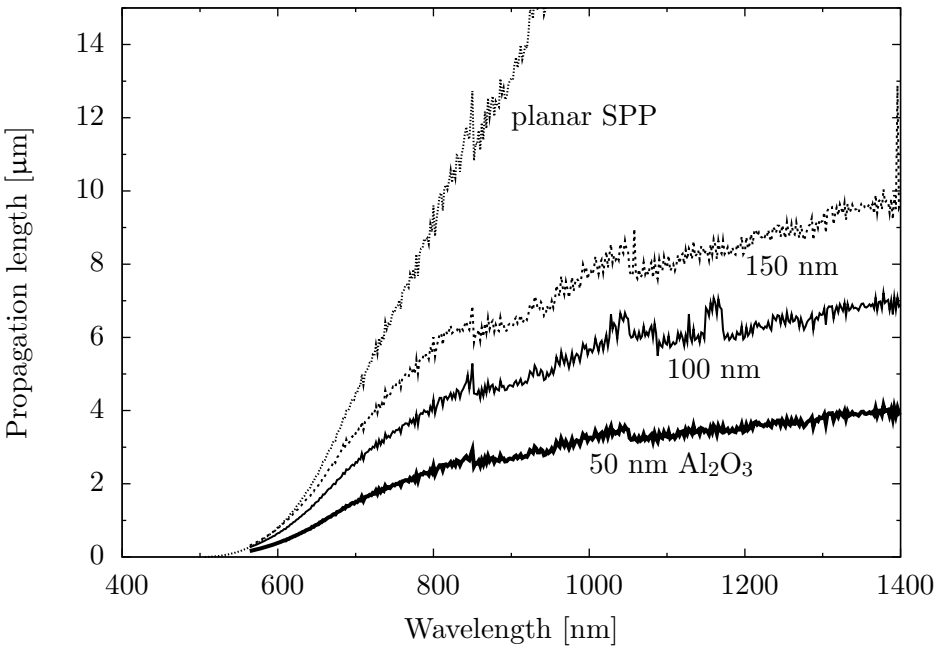

Figure 5.5: Calculated propagation length for the planar Au/Al_2O_3 surface plasmon and for the symmetric MIM $Au/Al_2O_3/Au$ surface plasmons based on measured dielectric constants for three Al_2O_3 thicknesses.

According to figure 5.5, the propagation length for the emission range of the Si nanocrystals (λ = 700–900 nm) is on the order of 5 µm. Using a thicker alumina layer would increase the propagation length, but the coupling between the two plasmons on both interfaces decreases.

For thicker insulator layers, the MIM geometry also supports multiple photonic waveguide modes. Figure 5.6 shows propagation lengths for optical modes as a function of insulator thickness in the MIM geometry for a free space wavelength $\lambda_{\text{free space}}$ = 800 nm. The calculation is based on the measured dielectric constants of the metal and the dielectric material (see figure 5.3). For thin insulator layers up to 175 nm, the symmetric plasmon mode is the only available optical mode with a propagation length larger than 100 nm. For larger thicknesses, also photonic waveguide modes appear. Experiments on electrical excitation of SPPs were performed using a layer thickness of 100 nm, so that only a single plasmonic mode can be expected. We have confirmed the absence of an optical waveguide for a 100 nm layer thickness by two separate mode solver programs.

The ALD process allows us to position the Si nanocrystals with high spatial resolution in the Al_2O_3 layer. To find the optimum position to place the Si nanocrystals we used a model by Ford and Weber [66]. Figure 5.7 shows the relative decay rate of a randomly oriented dipole into either SPPs or to quenching to the metal. The calculation also confirms that no coupling to spontaneous emission into photonic modes occurs. Figure 5.7 shows that to avoid quenching to the gold layers, the nanocrystals should be placed at least 10 nm from the interfaces.

5.3 Fabrication

The sample and the membrane structures were prepared as follows: a Si substrate was cleaned and the native oxide was etched, after which the wafer was immediately loaded into the vacuum system. By using atomic layer deposition (ALD), 20 nm of alumina was deposited onto the substrate. This required 245 ALD cycles with water and trimethylaluminum. The substrate temperature was 300 °C. Without breaking the vacuum, the wafer was transferred to a low-pressure chemical vapor deposition (LPCVD) reactor, where Si was deposited onto the sample by using Si_3H_8 as precursor gas. The process temperature was 325 °C. This procedure was repeated four times, so that four layers with Si nanocrystals in between the Al_2O_3 layers were deposited (see also chapter 4). Figure 5.8 shows an SEM micrograph of a crosscut through this membrane

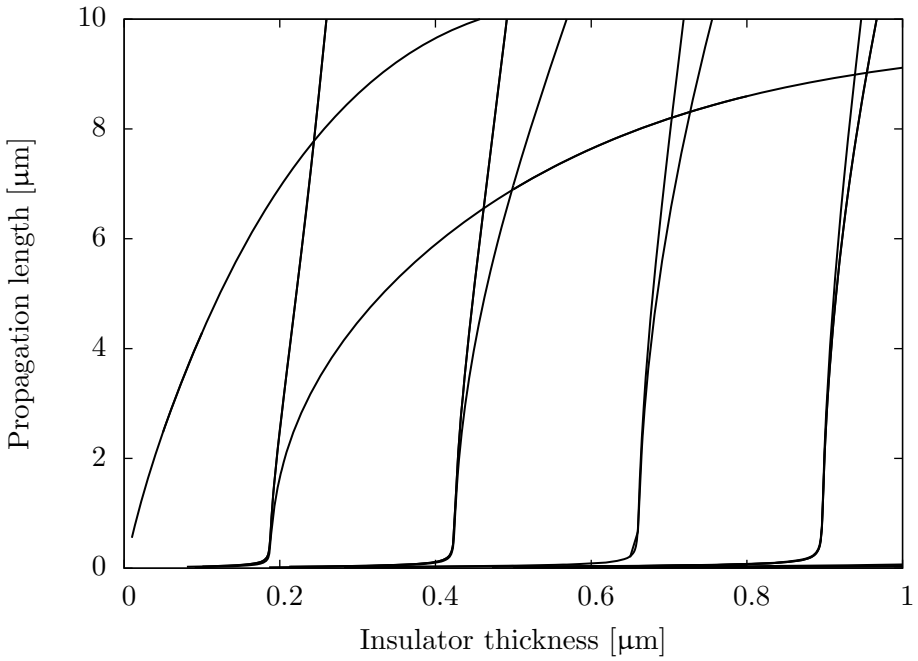

Figure 5.6: Propagation lengths for photonic and plasmonic modes in an MIM geometry as a function of the insulator thickness for a free space wavelength of $\lambda_{\text{freespace}} = 800$ nm. For thin structures (up to 175 nm), the symmetric plasmon mode is the only available mode with a propagation length larger than 100 nm.

structure.

After deposition of the active material, 250 nm of gold was sputter-coated onto the sample. At the backside of the wafer, 400 nm of SiO_2 was deposited by plasma-enhanced chemical vapor deposition (PECVD) and this oxide layer was patterned using optical lithography and a buffered HF etch solution. This oxide served as a hard mask for a tetra-methyl ammonium hydroxide (TMAH) etch solution. This solution selectively etches silicon anisotropically. The wafer was back-etched up to the alumina layer in order to create membranes of Al_2O_3 and gold. The backside etch was also used to create break-lines to dice the wafer later into 1×1 cm samples.

The wafer was "glued" with photoresist onto a pyrex carrier wafer for mechanical stability. A photoresist was spun onto the topside of the wafer and this layer was patterned by optical lithography. The pattern on the topside

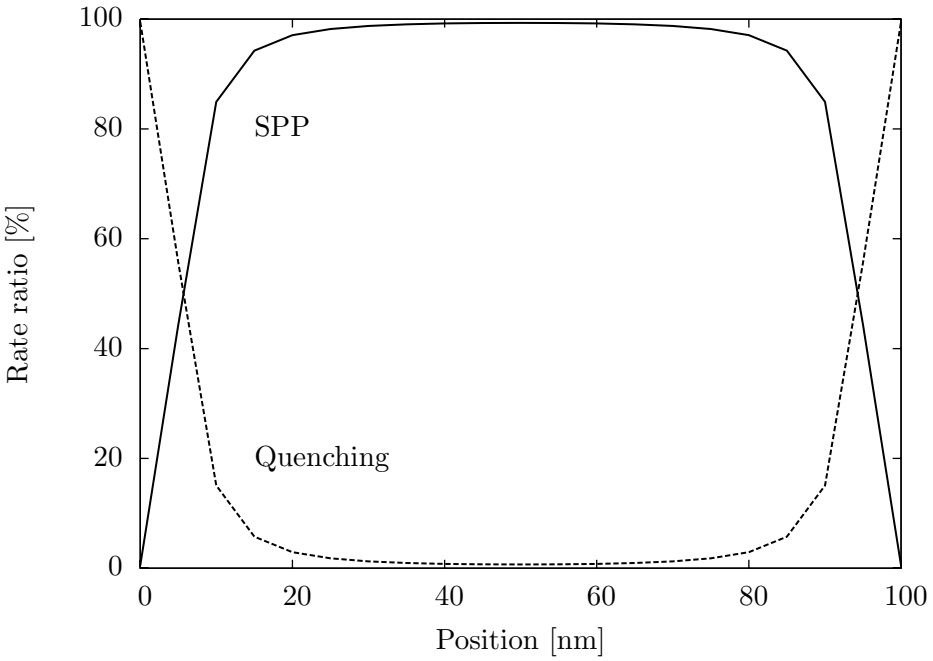

Figure 5.7: Relative decay rate of an optical emitter placed in a 100 nm thick alumina layer sandwiched between semi-infinite gold layers into either MIM surface plasmons or quenching to the metal, as a function of position in the alumina layer.

was aligned with the pattern on the backside. The 1×1 cm samples, with each four membrane-structures, were separated from the glass carrier wafer by using a surgical blade. With a wet gold etch (potassium iodine), the pattern on the topside was transferred into the gold. The pattern in the gold now consists of large rectangles ($\sim 2 \times 1$ mm) that cover the membranes. In order to bias the membranes individually, each rectangle covers only a single membrane. The remaining resist was removed and the samples were cleaned by soaking the samples several times in acetone, de-mineralized water, and propanol. By using a physical mask, the bottom side of the membranes and part of the silicon substrate were sputter-coated with 250 nm of gold.

With a focused ion beam system (FIB) the outline of a square was milled to create an electrically isolated gold square in the bottom side of the membrane, comparable to the isolation slit in section 3.2. The trench in the gold is 240 nm wide. By finite difference time domain (FDTD) simulations, we have estimated

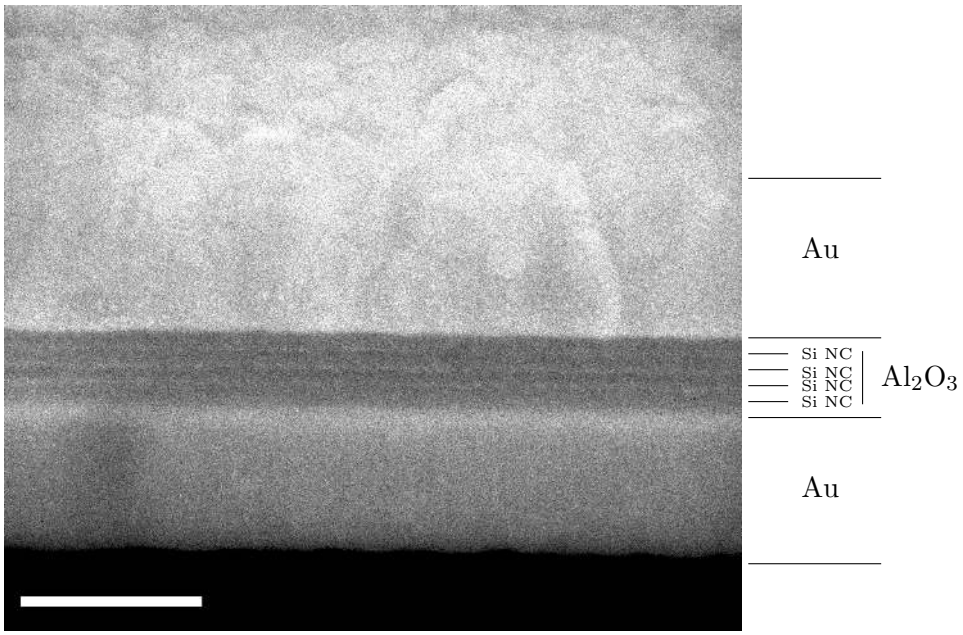

Figure 5.8: Cross section SEM image of the membrane structure. The top and bottom layers are sputtered gold films, the middle layer is composed of multilayers of Al_2O_3 and layers of Si nanocrystals. The scale bar is 250 nm.

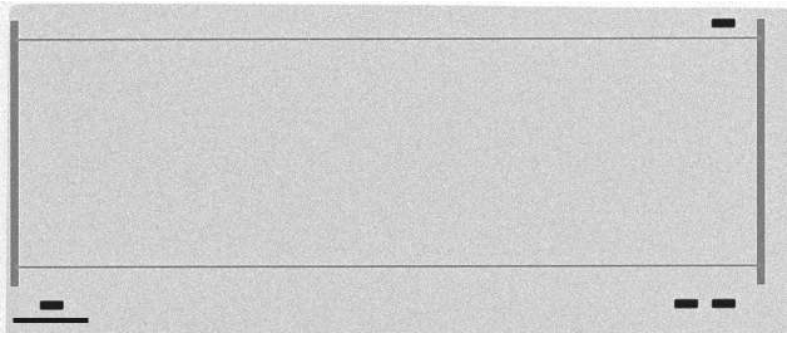

Figure 5.9: SEM image of backside of the membrane. The four black rectangles are alignment markers that are milled through the entire membrane stack. The scale bar in the bottom left corner is 10 µm.

the transmission loss for the SPP over the isolation slit to be 2 dB. Figure 5.9 shows an SEM image of this structure in the backside of the membrane. After this FIB-session, the sample was upturned, so a nanostructure could be milled into the topside. The outcoupling structure was milled in the gold on the topside, aligned with the electrically isolated square in the bottom side. The distance between the edge of the square and the outcoupling structure was varied from 1 to 10 µm to study the propagation lengths of the SPPs (see figure 5.10). The outcoupling structure to radiate SPPs into the far-field was optimized by using FDTD simulations. It consists of two 270 nm wide slits in the gold, separated by a 70 nm wide bar of gold. The inset of figure 5.10 shows a magnification of a single outcoupling structure.

5.4 Optical excitation of plasmons

In the MIM geometry, plasmons were first optically excited by illuminating the backside of the membrane with a white light source, similar as is presented in reference [78]. A 2 µm wide slit was created in the gold. The edges of the slit scatter the incident light partially in the MIM SPP mode. Plasmons propagate inside the MIM geometry and are reradiated into the far-field by outcoupling structures, as are shown in figure 5.10.

With an optical scanning confocal microscope, the light radiated by the outcoupling structures was measured. A linear polarizer was placed in the optical path to resolve the polarization of the light. Figure 5.11 shows the normalized polarized light intensity radiated by an outcoupling structure, as

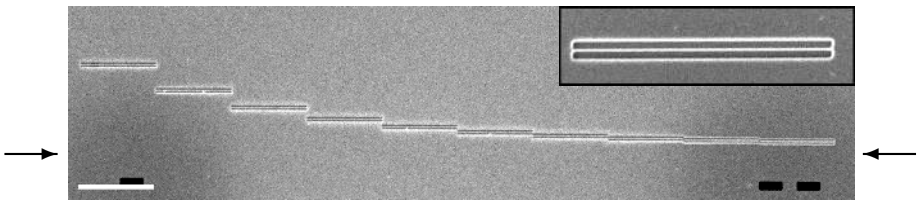

Figure 5.10: SEM image of the MIM plasmon waveguides taken from the top. The outcoupling structures in the top gold surface are clearly visible. The slits are 10 μm wide. The distance between the isolation slit (located at the bottom of the image, between the two arrows) and the outcoupling structure is systematically varied to map the surface plasmon propagation length. The three black squares on the bottom of the image are holes in the membrane to align top and bottom patterns. The scale bar is 10 μm. The inset on the top right shows a higher magnification of a single outcoupling structure.

a function of the polarizer angle. The emitted light shows a clear preferential polarization direction, which is perpendicular to the outcoupling structures. For a polarization angle which is parallel to the outcoupling structures, very little light is detected. The dashed line in figure 5.11 shows the normalized light intensity in a similar experiment, but with the sample 90 degrees rotated. The polarization angles for the maximum and minimum light intensities are now shifted by 90 degrees, showing that the outcoupling structures indeed show polarized emission in agreement with the expectation for reradiated SPPs.

Polarized light intensities of several outcoupling structures positioned at distances ranging from 0.5 to 5 μm from the slit in the bottom side were measured. Figure 5.12 shows the decay of light intensity for outcoupling structures further away from the excitation slit for three wavelength ranges. The measured intensity I is fitted to a single exponential decay function: $I = I_0 \exp(-x/L_{\text{prop}})$, with I_0 the intensity at the excitation slit, x the distance to excitation slit and L_{prop} the plasmon propagation length. The fits to the data are also plotted in figure 5.12. The measured intensities are normalized to I_0.

The propagation lengths obtained by the fit are shown in table 5.1. There is a good correspondence between the theoretical propagation lengths (obtained from the measured dielectric constants, see figure 5.5) and the propagation lengths obtained by the fit. This agreement, together with the polarization dependency shown in figure 5.11, is evidence of optically excited SPPs.

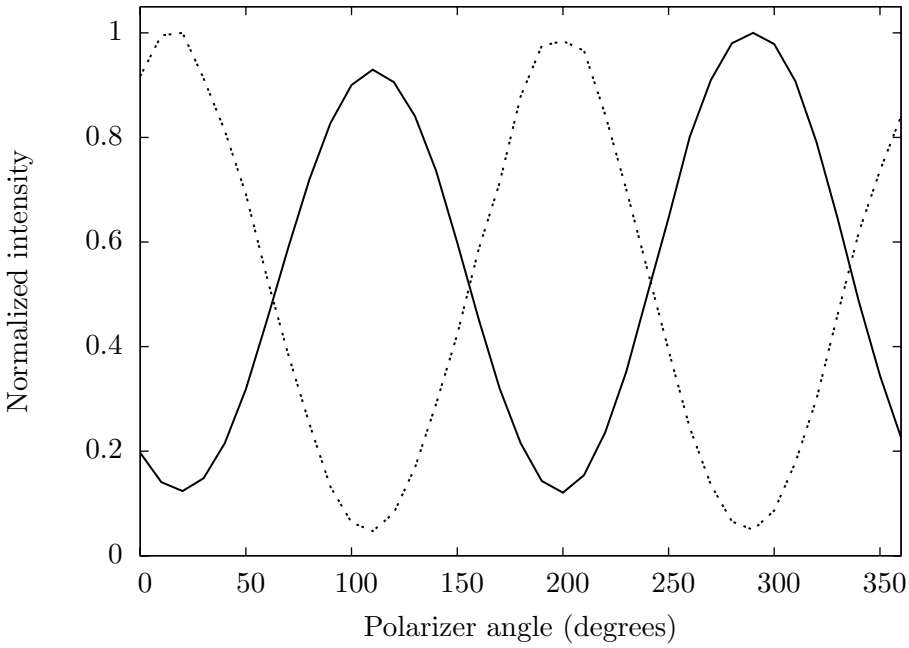

Figure 5.11: Normalized intensities of polarized light reradiated by an outcoupling structure (see figure 5.10) for different polarization angles. Solid line: polarizer parallel to the outcoupling structure at 20 and 200 degrees. Dashed line: shows the same measurement with the sample rotated by 90 degrees.

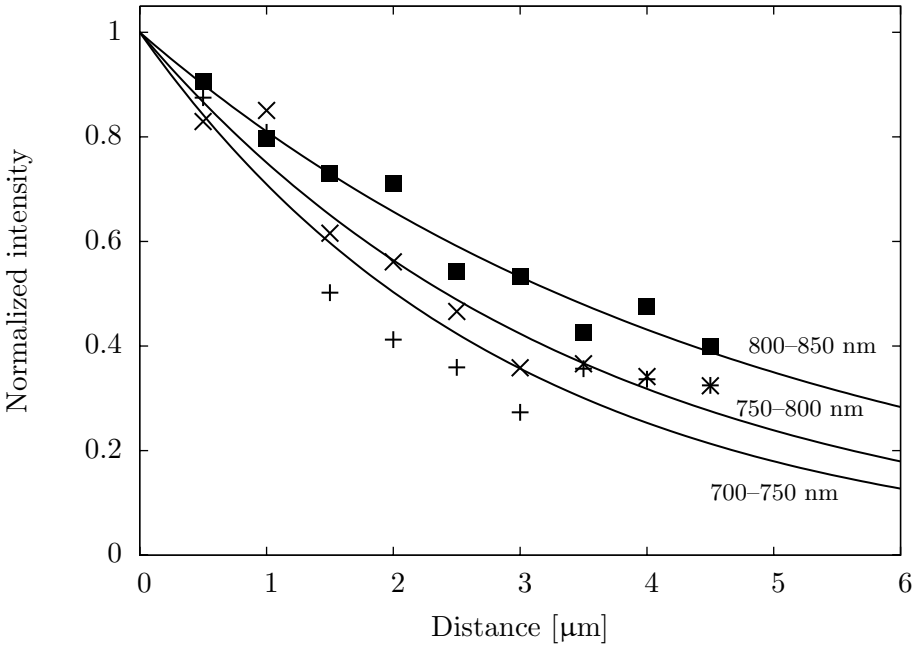

Figure 5.12: Intensity of reradiated light by outcoupling structures as a function of distance to the excitation slit in the bottom side for three wavelength ranges: 700–750 nm (+), 750–800 nm (×), and 800–850 nm (■). The lines show a single exponential fit to the data. The intensities are normalized to the fitted intensity at the excitation slit.

Table 5.1: Theoretical and experimental SPP propagation length.

Wavelength [nm]	Theoretical propagation length [μm]	Experimental propagation length [μm]
700–750	3.0	2.9 ± 0.5
750–800	3.8	3.5 ± 0.4
800–850	4.8	4.6 ± 0.4

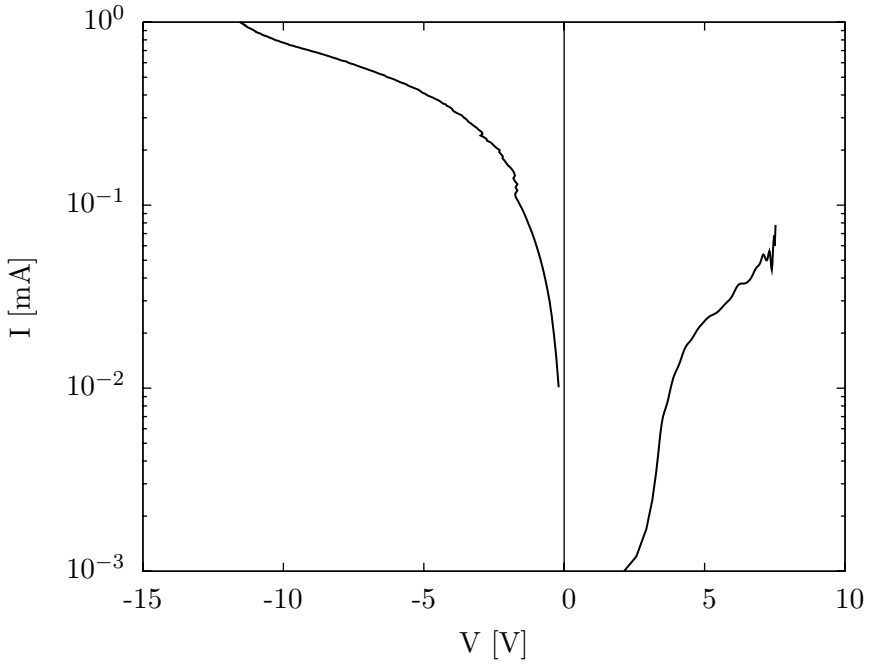

Figure 5.13: Current–voltage characteristic of the electrically excitable SPP source. A clear rectifying behavior is observed.

5.5 Electrical excitation of plasmons

Electrical contact to the gold layer on the top side of the sample shown in figure 5.10 was made by a probe needle. The electrical contact to the rear side was made by placing the sample onto a gold coated Si wafer. To bias the device, the sample was connected to a current-source. During the measurements, the conductivity increased due to resistive heating and the voltage thus varied during the measurement.

The electrically contacted sample was positioned under a 100× objective (NA = 0.73) with a long working distance (6.5 mm). The light collected by the objective was projected onto a CCD-camera to image the sample. A beam splitter in the optical path was used to enable white-light illumination for focusing and alignment of the sample.

The sample was biased to a current of 1 mA, which is caused by two parallel current paths: a path through the membrane (with an area on the order of 1×10^{-4} cm^2) and a leakage path through the Si substrate (with an area on

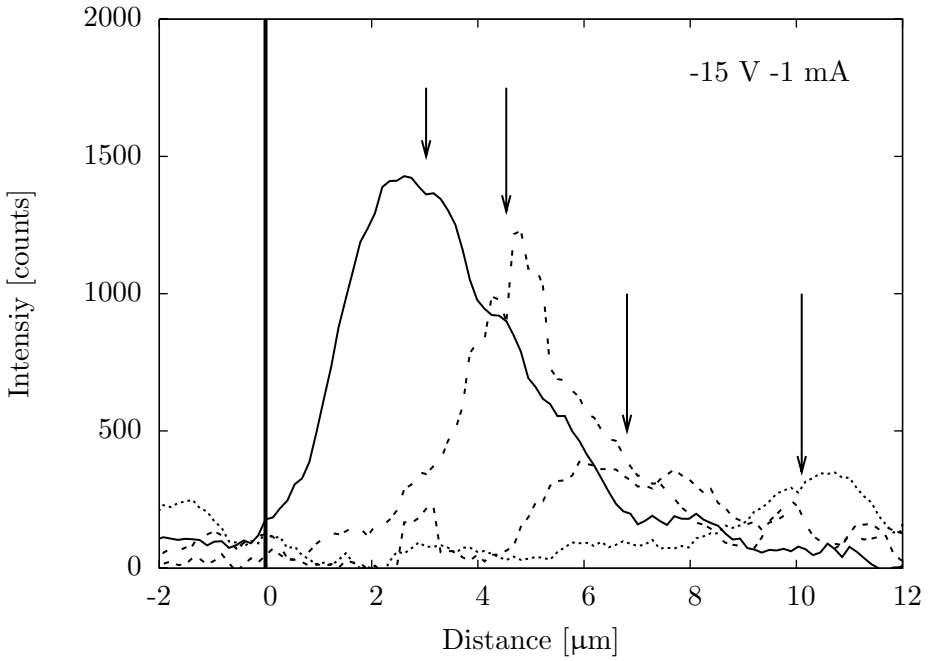

Figure 5.14: Light intensity collected from the plasmon waveguide with outcoupling slits for the MIM plasmon source under electrical excitation. Data is shown for four waveguides with outcoupling slits at different distances (indicated by arrows) from the incoupling slit (at position 0 μm).

the order of 200×10^{-4} cm^2). A current–voltage characteristic of the sample is shown in figure 5.13. A clear rectifying behavior is observed. For the optical measurements, the gold on the Al_2O_3 layer was negatively biased with respect to the gold contact on the rear side.

Figure 5.14 shows the light intensity collected by the CCD-camera as a function of distance taken across four different outcoupling slits. These line scans correspond to vertical directions in figure 5.10. The zero-position is set by the position of the slit in the bottom side of the membrane structure and was determined by using markers and SEM-images (see figures 5.9 and 5.10). The arrows show the position of the outcoupling structures. The line traces are summed over the width of the outcoupling structures to obtain an optimum signal–to–noise ratio. At each outcoupling structure, an increase in light intensity is observed. The intensity decreases when the outcoupling structure is further away from the isolation slit in the bottom side of the membrane.

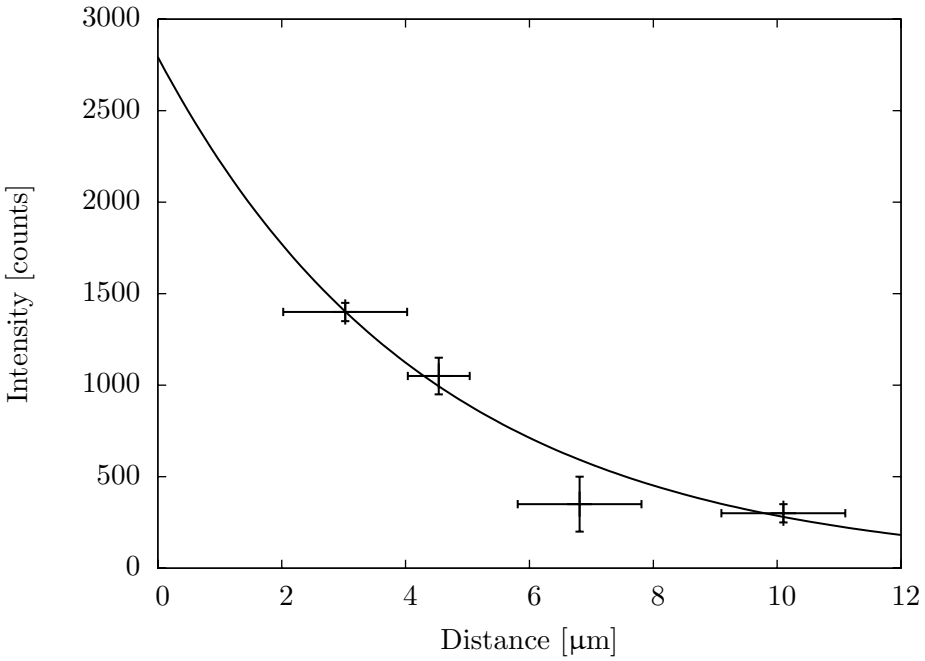

Figure 5.15: Measured light intensity of outcoupled SPPs (points) as a function of distance from the slit in the bottom Au layer of the membrane. The line shows a single exponential decay of intensity fitted to the data. The obtained propagation length is 4.4 ± 0.6 μm.

Since SPPs are the only available mode in the geometry, these observations are direct evidence for the generation of electrically excited SPPs that are coupled to the far-field.

From the position and the height of the peaks in the line traces from figure 5.14, an estimate for the MIM SPP propagation length L_{prop} can be obtained. Figure 5.15 shows the measured light intensities as a function of distance to the slit in the bottom side of the membrane. The figure also shows a single exponential decay function ($I = I_0 \exp(-x/L_{prop})$) that is fitted to the data with I_0 and L_{prop} as free parameters. The fitted propagation length is $L_{prop} = 4.4 \pm 0.6$ μm. This is in good agreement with the calculations in figure 5.5 which shows an average propagation length $L_{prop} = 4.5$ μm for the $\lambda = 550$–1000 nm range.

Figure 5.16 shows the spectrum of radiated SPPs by an outcoupling structure. The radiated SPPs from the sample were detected by a long working

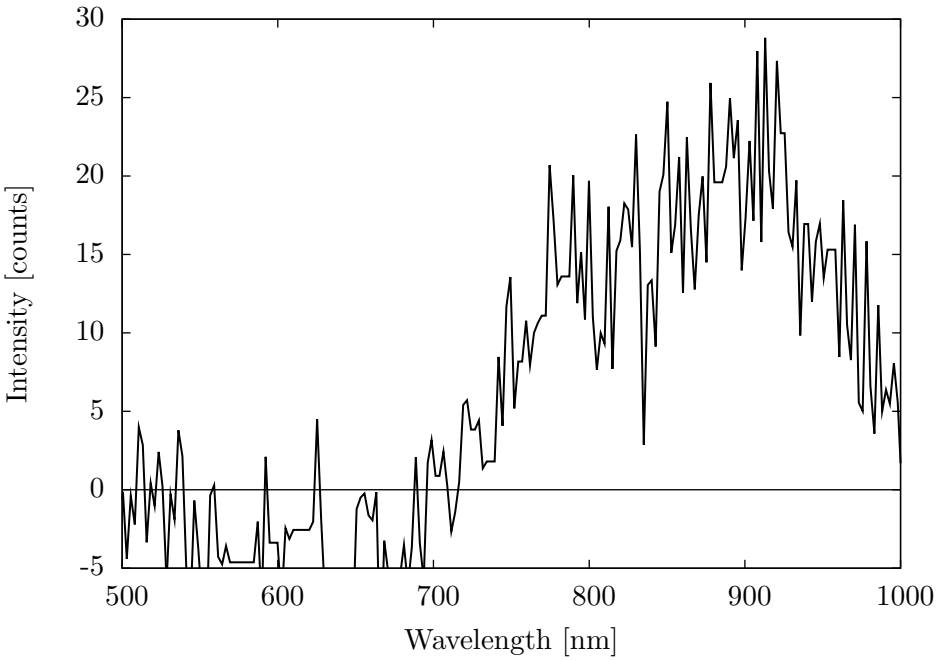

Figure 5.16: Spectrum of radiated SPPs by an outcoupling structure placed 1 µm away from the excitation pad.

distance objective (100×, NA = 0.73). A second lens (f = 15 cm) focussed the light onto the entrance slits of a spectrometer. A beam splitter was positioned in the parallel optical path for white light illumination for alignment and focussing of the sample onto the spectrometer.

The spectrum of radiated SPPs in figure 5.16 is clearly redshifted compared to the electroluminescence spectra shown in figure 4.5. This is consistent with the fact that short wavelength SPPs have a propagation length shorter than the distance to the outcoupling structure. Indeed, the propagation length for $\lambda_{\text{free space}} = 600$ nm is only $L_{\text{prop}} = 650$ nm (see figure 5.5).

5.6 Outlook

The MIM plasmon source can also be used to obtain a plasmon source in an insulator–metal (IM) structure. The fabrication for the planar geometry is similar as is discussed in section 5.3. In the final step of FIB milling in both

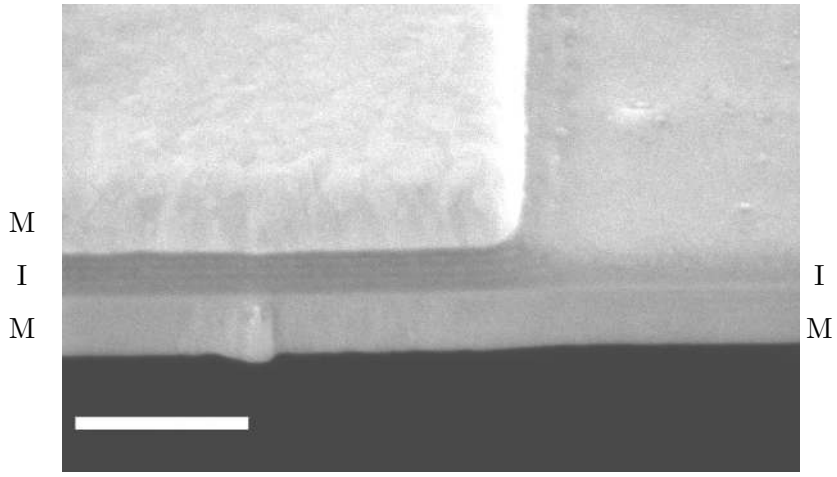

Figure 5.17: SEM image of an electrical IM SPP source in a membrane geometry. An MIM SPP is created on the left hand side and is converted into an IM SPP on the right hand side. The scale bar is 500 nm.

top and bottom side, the pattern is different from the MIM plasmon source. In the top side of the membrane the gold is removed up to the Al_2O_3 layer. Figure 5.17 shows an SEM image of the proposed structure. The MIM SPP source is used to electrically excite SPPs (left hand side of figure 5.17). The SPPs propagate until the edge of the top gold cladding layer. At the edge, the MIM SPPs are converted into IM SPPs. FDTD simulations show that the conversion efficiency between the two modes is about 50%. The remaining part of the MIM SPPs is reflected or scattered into the far field by the edge of the top gold cladding layer. Initial experiments to fabricate an electrical IM SPP source using this geometry show promising results.

5.7 Conclusions

An electrically excited source for SPPs was designed, fabricated and demonstrated based on a $Au/Al_2O_3/Au$ layer structure. The dispersion relation and the propagation length for the symmetric SPP mode of the MIM geometry were calculated based on measured values of the dielectric constants for gold

and alumina. At a free space wavelength of $\lambda = 800$ nm (1.55 eV), the SPP k-vector is 0.017 nm^{-1} ($\lambda_{SPP} = 370$ nm). The $1/e$ decay length for the SPP is 4.3 μm. For a 100 nm thick alumina layer, there are no other photonic modes in the MIM layer besides the SPP mode.

An alumina layer that was doped with silicon nanocrystals was sandwiched between two layers of gold to fabricate a metal–insulator–metal (MIM) geometry. This structure was realized by making use of a thin (600 nm thick) suspended alumina membrane. The MIM layers were first characterized by optical measurements. The propagation length and polarization state of light collected from outcoupling structures is consistent with the existence of MIM plasmon modes. The silicon nanocrystals were electrically excited by biasing gold layers on the top and the bottom side. The excited nanocrystals decay by generating SPPs. The sample was biased using a current-source to a current of 1 mA. Light emission from the outcoupling structures was detected with spectra peaking at $\lambda = 900$ nm. The light intensity decreased for larger distances of the outcoupling structure to the slit: an MIM SPP propagation length of $L_{prop} = 4.4 \pm 0.6$ μm was obtained, in agreement with calculations based on the measured dielectric constants. The data are evidence for electrically excited SPPs in an MIM geometry.

Chapter 6

Application outlook

In the past years, several useful applications of modified dispersion and nano-scale field concentration of surface plasmons have been proposed. All of these applications suffer from the impractical fact that optical excitation of surface plasmons was assumed, leading to bulky device designs. With the realization of the electrically excitable SPP source as is described in this thesis, device designs can be modified and made more practical. This chapter describes applications and designs with the electrical plasmon source incorporated.

6.1 Electrical SPP source with tapers

For sensing applications based on Raman spectroscopy, high electromagnetic field concentrations are needed to detect specific molecules with a sensitivity up to the single-molecule level [79]. By using surface plasmons to focus light to sub-wavelength spot-sizes, these high field concentrations can be obtained. MIM geometries confine the electromagnetic energy in the thin dielectric material. Strong confinement of the energy can also be obtained with SPPs in a taper geometry, where a plasmonic waveguide is tapered down to a needle-sharp tip [11]. Verhagen *et al.* experimentally demonstrated plasmon concentration by using a 2D taper in a plasmon waveguide [12].

The electrical plasmon sources as are described in this thesis can be equipped with a tapered waveguide. Figure 6.1 shows a cartoon of a possible geometry for such a device. On the left hand side, MIM plasmons are generated. The MIM plasmons are converted into planar IM plasmons and propagate along the taper which concentrates the plasmon intensity. A molecule that is positioned at the end of the taper can be excited by the concentrated light and thereby show an intensified fluorescence signal that could lead to the detection of the fluorescence of this molecule.

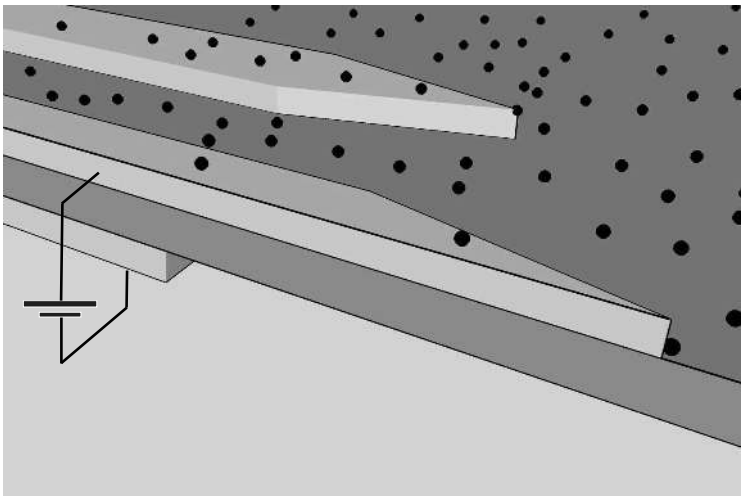

Figure 6.1: Schematic of a cross cut of a planar electrical surface plasmon source, ending in a taper to concentrate light at sub-wavelengths scales. The black dots represent molecules that are detected by optical spectroscopy.

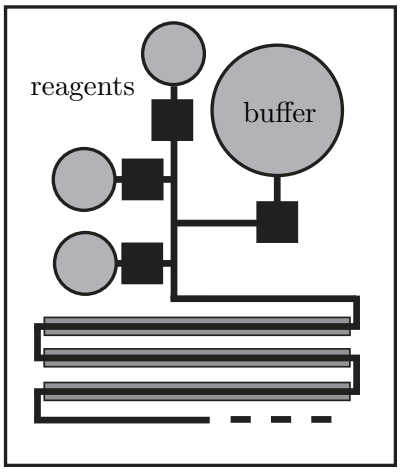

Figure 6.2: Schematic of a lab-on-a-chip with an integrated SPP source (dark gray boxes) along a micro-fluidic channel (black line). Electrically excited surface plasmons couple with the micro-fluidic channel. Micro-pumps and valves and storage tanks for reagents are also integrated on the chip.

6.2 SPP source for lab–on–a–chip

The lab–on–a–chip technology enables cheap and disposable devices for the sensitive detection of biochemical materials. Micro-fluidic channels transport liquids across the microchip for the detection of specific cells, enzymes or other molecules of interest. Lab-on-a-chip applications may lead to cheaper and faster detection and diagnoses of diseases [80].

Optical analysis is used for the detection of specific molecules in lab-on-a-chip devices [81]. In some configurations, e.g. the detection is based on luminescence of a dye attached to the molecule or enzyme. The optical excitation for this dye needs to be integrated onto the lab–on–a–chip [81]. Figure 6.2 shows a diagram of how electrically excited SPPs can be used as pump to excite this dye. The micro-fluidic channel is drawn as a meander across the chip. One side of the channel is composed of metal that is in intimate contact with the fluid, and supports SPPs. In this case, the metal can also be functionalized, so special label-molecules can attach to it. The chip also includes micro-pumps, valves and storage tanks.

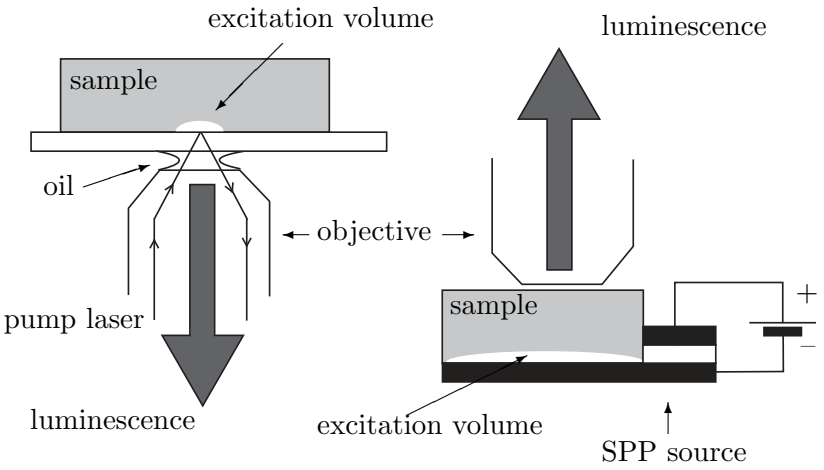

Figure 6.3: Conventional total internal reflection microscopy (left panel) where light from an excitation laser is reflected by the microscope slide and an evanescent wave excites a dye in the surface region of the sample. The luminescence is detected by the objective. The right panel shows how an electrically excitable SPP source can be used to excite a similar sample volume close to the interface. The luminescence can now be detected by a normal upright microscope.

6.3 Fluorescence microscopy at interfaces

In biophysical studies, a commonly used analytical technique is total internal reflection fluorescence (TIRF) microscopy [82]. This technique is used to selectively excite a dye near the interface of a sample with a microscope slide, and to eliminate background luminescence from deeper lying regions of the sample [83]. In an inverted optical microscope, light from an excitation laser is totally internally reflected by the microscope slide. The resulting evanescent wave inside the sample excites a dye only at the interface with the microscope slide. The luminescence from the dye is imaged by the microscope objective (see figure 6.3).

A similar small sample-volume can be excited by using an electrically excitable SPP source, as is presented in this thesis. The evanescent field of the SPPs only excites the dye at the interface. The luminescence can now be imaged by a normal upright microscope. The metal at the interface can also be functionalized so special label-molecules can attach to it.

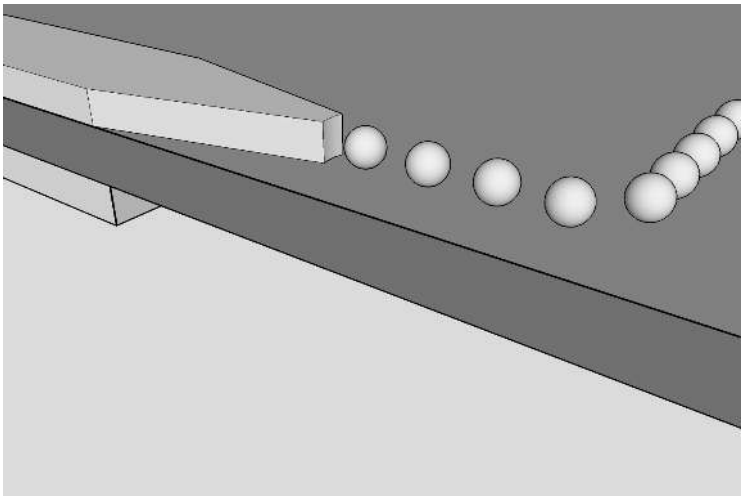

Figure 6.4: Schematic of a planar electrical surface plasmon source coupled to a metal particle array for applications in nanoscale integrated optics.

6.4 SPP detector

Besides an electrical source for SPPs, an SPP detector can be build with a similar structure [84]. The plasmon detector works opposite to the process described by figure 3.1. The plasmon energy is absorbed by quantum dots and creates excitons in the quantum dots. By using a bias across the active layer, the electron–hole pairs are separated and transported to the electrical contacts on both sides of the active layer leading to a photocurrent.

6.5 Electric SPP source with a particle array

A chain of metallic particles can guide light at sub-wavelength length scales [85, 86]. Also waveguide-bends, filters and splitters are proposed based on metal particle arrays that may be integrated into larger nanoscale integrated optical circuits [87]. The electrically generated SPP source presented in this thesis could be integrated in such circuits. An example for this geometry is shown in figure 6.4, where plasmons are generated electrically, concentrated by a tapered structure, and then confined into a metallic particle array.

6.6 On-chip signal transport by infrared plasmons

To make integrated circuits (IC's) more powerful and cost-effective, the dimensions of each transistor on the IC need to shrink. This means that the dimensions of signal leads on the chip must shrink as well. A smaller lead will lead to higher resistivities and capacities, which in turn lead to higher RC-times (slower response times) and more heating of the chip. These effects are unwanted.

The electrical SPP source presented in this thesis would be a potential candidate to generate signals on a chip (e.g. for the clock-signal distribution) [4, 6]. The fabrication techniques, especially for the SPP source presented in chapter 5, can be adapted to be compatible with standard CMOS processing techniques.

6.7 Quantum dot solar cell

To use of silicon quantum dots has been proposed to engineer the band gap in a tandem solar cell [88]. The absorption cross section of Si quantum dots was discussed in chapter 2 and was found to be on the order of 10^{-16} cm^2 at $\lambda = 700$ nm (it is strongly wavelength dependent [53]). The optical path length through the active layer, and thus the absorption of light by the quantum dots, can be increased by using a geometry in which the light propagates in the plane of the quantum dot doped layer instead of illuminating the layer with normal incidence.

Figure 6.5 shows a schematic of such a geometry, composed of a tandem structure in which different spectral ranges are coupled into layers with the corresponding band gaps. The incident light is converted into an SPP mode by a grating. The substrate is coated with a metal layer that supports the surface plasmons and acts as an electrical bottom contact. The skin depth into the dielectric material (with the Si quantum dots) increases for lower frequencies [1]. As a result, high frequency light is mostly absorbed in the bottom layer, that is doped with quantum dots with a high band gap. The lower frequencies are then absorbed in the top layer, with a lower band gap. The layered structure then has an optimized photovoltage that is determined by the series-circuit of the three active layers.

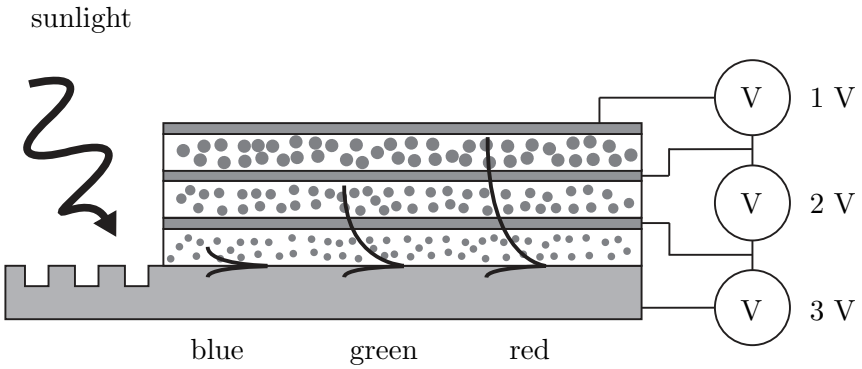

Figure 6.5: Schematic of a tandem solar cell based on quantum dots. Incident sunlight is converted into an SPP that travels in plane. The skin depth in the dielectric material for lower frequencies is larger than for higher frequencies. Smaller quantum dots can give higher V_{oc} values (e.g. 3 V) and are put on the bottom of the stack to absorb the shorter wavelength light. Larger quantum dots, which absorb longer wavelengths and give a smaller V_{oc} (e.g. 1 V), are put on top of the stack.

References

[1] H. Raether. *Surface plasmons on smooth and rough surfaces and on gratings*, Volume 111 of *Springer tracts in modern physics*. Springer-Verlag, 1988.

[2] W. L. Barnes, A. Dereux, and T. W. Ebbesen. *Surface plasmon subwavelength optics*. Nature, **424**(6950):824–830 (2003).

[3] H. A. Atwater. *The promise of plasmonics*. Scientific American, **296**(4):56–63 (2007).

[4] R. Zia, J. A. Schuller, A. Chandran, and M. L. Brongersma. *Plasmonics: the next chip-scale technology*. Materials Today, **9**(7-8):20–27 (2006).

[5] A. Polman. *Plasmonics applied*. Science, **322**(5903):868–869 (2008).

[6] E. Ozbay. *Plasmonics: merging photonics and electronics at nanoscale dimensions*. Science, **311**(5758):189–193 (2006).

[7] S. I. Bozhevolnyi, V. S. Volkov, E. Devaux, J.-Y. Laluet, and T. W. Ebbesen. *Channel plasmon subwavelength waveguide components including interferometers and ring resonators*. Nature, **440**(7083):508–511 (2006).

[8] H. Ditlbacher, J. R. Krenn, G. Schider, A. Leitner, and F. R. Aussenegg. *Two-dimensional optics with surface plasmon polaritons*. Applied Physics Letters, **81**(10):1762–1764 (2002).

[9] J. A. Dionne, L. A. Sweatlock, H. A. Atwater, and A. Polman. *Plasmon slot waveguides: towards chip-scale propagation with subwavelength-scale localization*. Physical Review B, **73**(3):035407 (2006).

[10] H. T. Miyazaki and Y. Kurokawa. *Squeezing visible light waves into a 3-nm-thick and 55-nm-Long plasmon cavity.* Physical Review Letters, **96**(9):097401 (2006).

[11] M. L. Stockman. *Nanofocusing of optical energy in tapered plasmonic waveguides.* Physical Review Letters, **93**(13):137404 (2004).

[12] E. Verhagen, L. Kuipers, and A. Polman. *Enhanced nonlinear optical effects with a tapered plasmonic waveguide.* Nanoletters, **7**(2):334–337 (2006).

[13] J. Homola, S. S. Yee, and G. Gauglitz. *Surface plasmon resonance sensors: review.* Sensors and Actuators B: Chemical, **54**(1-2):3–15 (1999).

[14] G. Roelkens, D. van Thourhout, and R. Baets. *High efficiency silicon-on-insulator grating coupler based on a poly-silicon overlay.* Optics Express, **14**(24):1162–11630 (2006).

[15] J. Kalkman, H. Gersen, L. Kuipers, and A. Polman. *Excitation of surface plasmons at a SiO_2/Ag interface by silicon quantum dots: Experiment and theory.* Physical Review B, **73**(7):075317 (2006).

[16] I. Gryczynski, J. Malicka, W. Jiang, H. Fischer, W. C. W. Chan, Z. Gryczynski, W. Grudzinski, and J. R. Lakowicz. *Surface-plasmon-coupled emission of quantum dots.* Journal of Physical Chemistry B, **109**(3):1088–1093 (2005).

[17] D. M. Koller, A. Hohenau, H. Ditlbacher, N. Galler, F. Reil, F.R. Aussenegg, A. Leitner, E. J. W. List, and J. R. Krenn. *Organic plasmon-emitting diode.* Nature Photonics, **2**(11):684–687 (2008).

[18] C. J. Yates, I. D. W. Samuel, P. L. Burn, S. Wedge, and W. L. Barnes. *Surface plasmon-polariton mediated emission from phosphorescent dendrimer light-emitting diodes.* Applied Physics Letters, **88**(16):161105 (2006).

[19] W. L. Barnes. *Fluorescence near interfaces: the role of photonic mode density.* Journal of Modern Optics, **45**(4):661–699 (1998).

[20] S. M. Sze. *Physics of semiconductor devices.* John Wiley & Sons, New York, 2nd edition, 1981.

[21] M. A. Green, J. Zhao, A. Wang, P. J. Reece, and M. Gal. *Efficient silicon light-emitting diodes.* Nature, **412**:805–808 (2001).

[22] A. G. Cullis and L. T. Canham. *Visible light emission due to quantum size effects in highly porous crystalline silicon.* Nature, **353**(6342):335–338 (1991).

[23] M. L. Brongersma, A. Polman, K. S. Min, E. Boer, T. Tambo, and H. A. Atwater. *Tuning the emission wavelength of Si nanocrystals in SiO_2 by oxidation.* Applied Physics Letters, **72**(20):2577–2579 (1998).

[24] T. Fischer, V. Petrova-Koch, K. Shcheglov, M. S. Brandt, and F. Koch. *Continuously tunable photoluminescence from Si^+–implanted and thermally annealed SiO_2 films.* Thin Solid Films, **276**(1–2):100–103 (1996).

[25] M. S. Hybertsen. *Absorption and emission of light in nanoscale silicon structures.* Physical Review Letters, **72**(10):1514–1517 (1994).

[26] M. V. Wolkin, J. Jorne, P. M. Fauchet, G. Allan, and C. Delerue. *Electronic states and luminescence in porous silicon quantum dots: the role of oxygen.* Physical Review Letters, **82**(1):197–200 (1999).

[27] F. Iacona, G. Franzò, and C. Spinella. *Correlation between luminescence and structural properties of Si nanocrystals.* Journal of Applied Physics, **87**(3):1295–1303 (2000).

[28] G. Franzò, A. Irrera, E. C. Moreira, M. Miritello, D. Sanfilippo, G. Di Stefano, P. G. Fallica, and F. Priolo. *Electroluminescence of silicon nanocrystals in MOS structures.* Applied Physcics A, **74**(1):1–5 (2002).

[29] R. J. Walters, G. I. Bourianoff, and H. A. Atwater. *Field-effect electroluminescence in silicon nanocrystals.* Nature Materials, **1**(4):143–146 (2002).

[30] J. Valenta, N. Lalic, and J. Linnros. *Electroluminescence of single silicon nanocrystals.* Applied Physics Letters, **84**(9):1459–1461 (2004).

[31] M. Sopinskyy and V. Khomchenko. *Electroluminescence in SiO_x films and SiO_x-film-based systems.* Current Opinion in Solid State & Materials Science, **7**(2):97 (2003).

[32] A. Irrera, D. Pacifici, M. Miritello, G. Franzò, F. Priolo, F. Iacona, D. Sanfilippo, G. Di Stefano, and P. G. Fallica. *Excitation and de-excitation properties of silicon quantum dots under electrical pumping.* Applied Physics Letters, **81**(10):1866–1868 (2002).

[33] L.-Y. Chen, W.-H. Chen, and F. C.-N. Hong. *Visible electroluminescence from silicon nanocrystals embedded in amorphous silicon nitride matrix.* Applied Physics Letters, **86**(19):193506 (2005).

[34] K. S. Min, K. V. Shcheglov, C. M. Yang, H. A. Atwater, M. L. Brongersma, and A. Polman. *Defect-related versus excitonic visible light emission from ion beam synthesized Si nanocrystals in SiO_2.* Applied Physics Letters, **69**(14):2033–2035 (1996).

[35] I. Brunets, A. A. I. Aarnink, A. Boogaard, A. Y. Kovalgin, R. A. M. Wolters, J. Holleman, and J. Schmitz. *Low-temperature LPCVD of Si nanocrystals from disilane and trisilane (Silcore ®) embedded in ALD-alumina for non-volatile memory devices.* Surface & Coatings Technology, **201**(22–23):9209–9214 (2007).

[36] T. Orii, M. Hirasawa, and T. Seto. *Tunable, narrow-band light emission from size-selected Si nanoparticles produced by pulsed-laser ablation.* Applied Physics Letters, **83**(16):3395–3397 (2003).

[37] E. D. van Hattum, A. Palmero, W. M. Arnoldbik, and F. H. P. M. Habraken. *Experimental characterization of the deposition of silicon suboxide films in a radiofrequency magnetron reactive sputtering system.* Surface and Coatings Technology, **188-189**:399–403 (2004).

[38] M. Rosso-Vasic, E. Spruijt, B. van Lagen, L. De Cola, and H. Zuilhof. *Alkyl-functionalizes oxide-free silicon nanoparticles: synthesis and optical properties.* Small, **4**(10):1835–1841 (2008).

[39] G. Das, L. Bettotti, F. De Angelis, G. Mariotto, L. Pavesi, E. Di Fabrizio, and G. D. Soraru. *Si-nanocrystals/SiO_2 thin films opbtained by pyrolysis of sol-gel precursors.* Thin Solid Films, **516**:6804–6807 (2008).

[40] W. Kern, editor. *Handbook of semiconductor wafer cleaning technology.* Noyes Publications, New Jersey, 1993.

[41] T. Shimizu-Iwayama, S. Nakao, and K. Saitoh. *Visible photoluminescence in Si^+-implanted thermal oxide films on crystalline Si.* Applied Physics Letters, **65**(14):1814–1816 (1994).

[42] C. M. Herzinger, B. Johs, W. A. McGahan, J. A. Woollam, and W. Paulson. *Ellipsometric determination of optical constants for silicon and thermally grown silicon dioxide via a multi-sample, multi-wavelength, multi-angle investigation.* Journal of Applied Physics, **83**(6):3323–3336 (1998).

[43] E. D. Palik, editor. *Handbook of optical constants of solids*, Volume 1. Academic Press, Inc., New York, 1985.

[44] K.-J. Lee, T.-D. Kang, H. Lee, S. H. Hong, S.-H. Choi, T.-Y. Seong, K. J. Kim, and D. W. Moon. *Optical properties of SiO_2/nanocrystalline Si multilayers studied using spectroscopic ellipsometry.* Thin Solid Films, **476**(1):196 – 200 (2005).

[45] D.E. Aspnes. *Optical properties of thin films.* Thin Solid Films, **89**(3):249 – 262 (1982).

[46] J. Linnros, N. Lalic, A. Galeckas, and V. Grivickas. *Analysis of the stretched exponential photoluminescence decay from nanometer-sized silicon crystals in SiO_2.* Journal of Applied Physics, **86**(11):6128–6134 (1999).

[47] R. J. Walters, J. Kalkman, A. Polman, H. A. Atwater, and M. J. A. de Dood. *Photoluminescence quantum efficiency of dense silicon nanocrystal ensembles in SiO_2.* Physical Review B, **73**:132302 (2006).

[48] F. Priolo, G. Franzò, D. Pacifici, V. Vinciguerra, F. Iacona, and A. Irrera. *Role of the energy transfer in the optical properties of undoped and Er-doped interacting Si nanocrystals.* Journal of Applied Physics, **89**(1):264–272 (2001).

[49] S. Miura, T. Nakamura, M. Fujii, M. Inui, and S. Hayashi. *Size dependence of photoluminescence quantum efficiency of Si nanocrystals.* Physical Review B, **73**(24):245333 (2006).

[50] C. Garcia, B. Garrido, P. Pellegrino, R. Ferre, J. A. Moreno, J. R. Morante, L. Pavesi, and M. Cazzanelli. *Size dependence of lifetime and absorption cross section of Si nanocrystals embedded in SiO_2.* Applied Physics Letters, **82**(10):1595–1597 (2003).

[51] R. Loudon. *The quantum theory of light.* Clarendon press, 1973.

[52] C. P. Lindsey and G. D. Patterson. *Detailed comparison of the Williams-Watts and Cole-Davidson functions.* Journal of Chemical Physics, **73**(7):3348–3357 (1980).

[53] D. Kovalev, J. Diener, H. Heckler, G. Polisski, N. Künzner, and F. Koch. *Optical absorption cross sections of Si nanocrystals.* Physical Review B, **61**(7):4485–4487 (2000).

[54] L. Qian, F. Teng, Z. Xu, S. Yang, Y. Hou, and X. Xu. *Electroluminescence and its excitation mechanism of SiO_x films deposited by electron-beam evaporation.* Physica B: Condensed Matter, **403**(12):1975–1978 (2008).

[55] M. Born and E. Wolf. *Principles of optics.* Cambridge University Press, reprinted 7^{th} edition edition, 1999.

[56] S. Kim, Y. M. Park, S.-H. Choi, and K. J. Kim. *Origin of cathodoluminescence from Si nanocrystal/SiO_2 multilayers.* Journal of Applied Physics, **101**(3):034306 (2007).

[57] L. H. Abuhassan, M. R. Khanlary, P. Townsend, and M. H. Nayfeh. *Cathodoluminescence of small silicon nanoparticles under electron-beam excitation.* Journal of Applied Physics, **97**(10):104314 (2005).

[58] J. T. van Wijngaarden. Cathodoluminescence imaging spectroscopy on plasmonic structures. Master's thesis, Utrecht University, 2005. This thesis can be downloaded from `http://www.erbium.nl`.

[59] F. Ziegler, J. Biersack, and U. Littmark. *The stopping and range of ions in solids.* Pergamon Press, New York, 1985.

[60] MicroChem Corp. NANO$^{\text{TM}}$PMMA and copolymer resist product data sheet. `http://www.microchem.com/products/pdf/PMMA_Data_Sheet.pdf`.

[61] A. Polman. *Erbium implanted thin film photonic materials.* Journal of Applied Physics, **82**(1):1–39 (1997).

[62] S. Lombardo, S. U. Campisano, G. N. van den Hoven, A. Cacciato, and A. Polman. *Room-temperature luminescence from Er-implanted semi-insulating polycrystalline silicon.* Applied Physics Letters, **63**(14):1942–1944 (1993).

[63] J. Kalkman, H. Gersen, L. Kuipers, and A. Polman. *Excitation of surface plasmons at a SiO_2/Ag interface by silicon quantum dots: experiment and theory.* Physcial Review B, **73**:075317 (2006).

[64] J. Seidel, F. I. Baida, L. Bischoff, B. Guizal, S. Grafström, D. Van Labeke, and L. M. Eng. *Coupling between surface plasmon modes on metal films.* Physical Review B, **69**(12):121405 (2004).

[65] T. Nikolajsen, K. Leosson, and S. I. Bozhevolnyi. *Surface plasmon polariton based modulators and switches operating at telecom wavelengths.* Applied Physics Letters, **85**(24):5833–5835 (2004).

[66] G. W. Ford and W. H. Weber. *Electromagnetic interactions of molecules with metal surfaces.* Physics Reports (Review Section of Physics Letters), **113**(4):195–287 (1984).

[67] K. H. Drexhage. *Influence of a dielectric interface on fluorescence decay time.* Journal of Luminescence, **1-2**:693–701 (1970).

[68] W. H. Weber and C. F. Eagen. *Energy transfer from an excited dye molecule to the surface plasmons of an adjacent metal.* Optics Letters, **4**(8):236 (1979).

[69] T. Förster. *Zwischenmolekulare Energiewanderung und Fluoreszenz.* Annalen der Physik, **437**(2):55–75 (1948).

[70] J. Kalkman. *Controlled spontaneous emission in erbium-doped microphotonic materials.* PhD thesis, Utrecht University, 2005.

[71] J. A. Dionne, L. A. Sweatlock, H. A. Atwater, and A. Polman. *Planar metal plasmon waveguides: frequency-dependent dispersion, propagation, localization, and loss beyond the free electron model.* Physical Review B, **72**:075405 (2005).

[72] E. Snoeks, A. Lagendijk, and A. Polman. *Measuring and modifying the spontaneous emission rate of erbium near an interface.* Physical Review Letters, **74**(13):2459–2462 (1995).

[73] D. I. Tetelbaum, O. N. Gorshkov, A. V. Ershov, A. P. Kasatkin, V. A. Kamin, A. N. Mikhaylov, A. I. Belov, D. M. Gaponova, L. Pavesi, L. Ferraioli, T. G. Finstad, and S. Foss. *Influence of the nature of oxide matrix on the photoluminescence spectrum of ion-synthesized silicon nanostructures.* Thin Solid Films, **515**(1):333–337 (2006).

[74] C. J. Park, Y. H. Kwon, Y. H. Lee, T. W. Kang, H. Y. Cho, Sung Kim, Suk-Ho Choi, and R. G. Elliman. *Origin of luminescence from Si^--implanted $(1\bar{1}02)$ Al_2O_3.* Applied Physics Letters, **84**(14):2667–2669 (2004).

[75] R. J. Walters. *Silicon nanocrystals for silicon photonics.* PhD thesis, California Institute of Technology, Pasadena, California, 2007.

[76] E. Verhagen, J. A. Dionne, L. Kuipers, H. A. Atwater, and A. Polman. *Near-field visualization of strongly confined surface plasmon polaritons in metal–insulator–metal waveguides.* Nanoletters, **8**(9):2925–2929 (2008).

[77] G. Winter, W. A. Murray, S. Wedge, and W. L. Barnes. *Spontaneous emission from within a metal-clad cavity mediated by coupled surface plasmon-polaritons.* Journal of Physics: Condensed Matter, **20**(30):304218 (2008).

[78] J. A. Dionne, H. J. Lezec, and H. A. Atwater. *Highly confined photon transport in subwavelength metallic slot waveguides.* Nanoletters, **6**(9):1928–1932.

[79] K. Kneipp, Y. Wang, H. Kneipp, L. T. Perelman, I. Itzkan, R. R. Dasari, and M. S. Feld. *Single molecule detection using surface-enhanced Raman scattering (SERS).* Physical Review Letters, **78**(9):1667–1670 (1997).

[80] P. Yager, T. Edwards, E. Fu, K. Helton, K. Nelson, M. R. Tam, and B. H. Weigl. *Microfluidic diagnostic technologies for global public health.* Nature, **442**(7101):412–418 (2006).

[81] H. Craighead. *Future lab-on-a-chip technologies for interrogating individual molecules.* Nature, **442**(7101):387–383 (2006).

[82] R. Narayanaswamy and O. S. Wolfbeis, editors. *Optical sensors: industrial, environmental and diagnostic applications*, Volume 1 of *Springer series on chemical sensors and biosensors.* Springer-Verlag, 2004.

[83] D. Axelrod, T. P. Burghardt, and N. L. Thompson. *Total internal reflection fluorescence.* Annual Review of Biophysics and Bioengineering, **13**:247–268 (1984).

[84] H. Ditlbacher, F. R. Aussenegg, J. R. Krenn, B. Lamprecht, G. Jakopic, and G. Leising. *Organic diodes as monolithically integrated surface plasmon polariton detectors.* Applied Physics Letters, **89**(16):161101 (2006).

[85] M. Quinten, A. Leitner, J. R. Krenn, and F. R. Aussenegg. *Electromagnetic energy transport via linear chains of silver nanoparticles.* Optics Letters, **23**(17):1331–1333 (1998).

[86] A. F. Koenderink, R. de Waele, J. C. Prangsma, and A. Polman. *Experimental evidence for large dynamic effects on the plasmon dispersion of subwavelength metal nanoparticle waveguides.* Physical Review B, **76**:201403 (2007).

[87] M. L. Brongersma, J. W. Hartman, and H. A. Atwater. *Electromagnetic energy transfer and switching in nanoparticle chain arrays below the diffraction limit.* Physical Review B, **62**(24):R16356–R16359 (2000).

[88] G. Conibeer, M. Green, R. Corkish, Y. Cho, E.-C. Cho, C.-W. Jiang, T. Fangsuwannarak, E. Pink, Y. Huang, T. Puzzer, T. Trupke, B. Richards, A. Shalav, and K.-L. Lin. *Silicon nanostructures for third generation photovoltaic solar cells.* Thin Solid Films, **511-512**:654–662 (2006).

Summary

A surface plasmon polariton (SPP) is an electromagnetic wave propagating at the interface between a metal and a dielectric material. The two-dimensional confinement of SPPs and the tunability of their dispersion enable optical functionality that cannot be achieved with regular dielectrics. Several novel concepts for sensing and opto-electronic integration based on SPPs have been proposed. In nearly all applications, as well as experiments based on SPPs, far-field excitation of SPPs is used, leading to bulky device designs. This thesis presents an electrically excitable source for SPPs that can be integrated in small, chip-size devices to enable the full application potential of SPPs. The device is based on a dielectric/metal geometry in which silicon quantum dots are placed in the near-field of the SPP mode. The quantum dots are electrically excited and decay by the generation of SPPs.

Chapter 2 describes Si quantum dots in silica made by a magnetron sputtering technique, followed by annealing. From photoluminescence spectra as well as lifetime measurements we conclude that well-passivated Si quantum dots with quantum confined luminescence around $\lambda = 800$ nm can be made. An electrical injection geometry is presented and electroluminescence is observed around $\lambda = 650$ nm under a bias of 15–30 V. Strong bleaching of the quantum dot luminescence is observed under 0.5–20 keV electron beam irradiation, which has a potential consequence for the use of electron beam lithography in nanofabrication of structures with Si quantum dots.

In chapter 3 we describe the design and the fabrication of an electrically excitable plasmon source based on an insulator–metal–insulator (IMI) geometry. The coupling of quantum dots to the SPP mode was studied theoretically

by using a model developed by Ford and Weber. For quantum dots spaced 20–200 nm away from the metal surface, more than 50% of the decay is into SPPs. An IMI SPP geometry for electrical excitation was fabricated using gold and silica doped with Si quantum dots as dielectric material. An IMI SPP source in the infrared region was fabricated by incorporating erbium in the dielectric material. Using an SPP waveguide coupled to the source, with suitable engineered outcoupling gratings, we observed the propagation and outcoupling of electrically excited SPPs. SPPs propagating along the waveguide have a transverse polarization and increased propagation for larger wavelength as expected from theory.

The optical properties of Si quantum dots in alumina are described in chapter 4. This material is deposited by using CMOS compatible, low-temperature techniques of atomic layer deposition (ALD) and low pressure chemical vapor deposition (LPCVD). Quantum-confined photo- and electroluminescence is observed at $\lambda = 700$–900 nm. The luminescence quantum efficiency is small (0.3%), presumably due to poor passivation.

Chapter 5 descirbes how this material is used in a novel metal–insulator–metal (MIM) geometry. SPPs are generated through the electrical excitation of the nanocrystals, propagate inside the MIM geometry and are radiated into the far-field by an outcoupling structure. The measured plasmon propagation length and the polarization state of the outcouples light are in agreement with theory.

The last chapter reports on several application ideas for the electrical SPP sources presented in this thesis. Integrated lab–on–a–chip devices, plasmonic (bio)sensors, nanoscale photonic integrated circuits, and a novel quantum dot solar cell geometry are proposed.

Samenvatting in het Nederlands

Een oppervlakteplasmonpolariton (OPP) is een elektromagnetische golf die zich voorplant aan het scheidingsvlak van een metaal met een diëlectricum. Het tweedimensionale karakter van een OPP en de mogelijkheid om de dispersierelatie aan te passen, maken een functionaliteit mogelijk die niet bereikbaar is met reguliere diëlectrische structuren. Verschillende nieuwe concepten voor sensoren en opto-elektronische integratie gebaseerd op OPP's zijn reeds gesuggereerd. In bijna alle toepassingen en experimenten gebaseerd op OPP's, worden verre-veld technieken gebruikt voor de excitatie van OPP's, wat leidt tot grote geometrieën. Dit proefschrift presenteert een elektrische bron voor OPP's die geïntegreerd kan worden in kleine apparaten ter grootte van een computerchip die de volle mogelijkheden benutten van OPP's. Het ontwerp is gebaseerd op een metaal/diëlectricum geometrie, waar silicium kwantumdots zijn geplaatst in het nabije veld van de OPP-mode. De kwantumdots worden elektrisch geëxciteerd en vervallen door OPP's te genereren.

Hoofdstuk 2 beschrijft Si kwantumdots in silica gemaakt door een magnetronsputtering-techniek, gevolgd door een anneal-stap. Uit fotoluminescentiespectra en levensduurmetingen hebben we geconcludeerd dat goed-gepassiveerde Si kwantumdots gemaakt kunnen worden, die een luminescentie door kwantumopsluiting geven rond een golflengte van $\lambda = 800$ nm. We presenteren een geometrie voor elektrische injectie van lading in deze kwantumdots. We hebben elektroluminescentie waargenomen rond $\lambda = 650$ nm, door een spanning van 15 – 30 V over de structuur te zetten. Sterke bleking van de kwantumdots is waargenomen onder elektronenbestraling met een energie van

0,5 – 20 keV, wat mogelijk gevolgen heeft voor het gebruik van elektronenbundellithografie in de nanofabricage van structuren met Si kwantumdots.

In hoofdstuk 3 beschrijven we het ontwerp en de fabricage van een elektrisch exciteerbare bron voor plasmonen, gebaseerd op een isolator–metaal–isolator (IMI) geometrie. De koppeling van de kwantumdots naar de OPP-mode is theoretisch bestudeerd met een model van Ford en Weber. Voor kwantumdots op een afstand van 20 tot 200 nm van het metaaloppervlak, is het verval voor meer dan 50% naar de OPP-mode. Een IMI-geometrie voor elektrische excitatie werd gemaakt met goud en met Si kwantumdots gedoteerd silica als diëlectrisch materiaal. Een IMI-OPP-bron in het infrarode gebied is gemaakt door erbium in het diëlectrische materiaal te plaatsen. Door OPP-golfgeleiders aan de bron te koppelen hebben we de voorplanting en de uitkoppeling van OPP's geobserveerd. OPP's die over de golfgeleider propageren, hebben een transversale polarisatie en de propagatielengte neemt toe voor grotere golflengtes, hetgeen in overeenstemming is met de theorie.

De optische eigenschappen van Si kwantumdots in alumina worden beschreven in hoofdstuk 4. Dit materiaal is gedeponeerd door CMOS-compatibele, lage-temperatuur-technieken van atomaire laagdepositie en lage-druk chemische dampdepositie. Foto- en elektroluminescentie uit kwantumopsluiting is waargenomen in het golflengtegebied λ = 700–900 nm. Waarschijnlijk door een gebrek aan goede passivatie is de efficiëntie van de lumeniscentie door kwantumopsluiting laag (0,3%).

In hoofdstuk 5 wordt beschreven hoe dit materiaal wordt gebruikt in een metaal–isolator–metaal (MIM) geometrie. OPP's worden gegenereerd door elektrisch aangeslagen Si kwantumdots en propageren binnenin de MIM structuur. Zij worden uiteindelijk naar het verre veld gestraald door uitkoppelstructuren. De gemeten propagatielengte en de polarisatie van het uitgestraalde licht zijn in goede overeenstemming met de theorie.

In het laatste hoofdstuk van dit proefschrift worden verschillende ideeën gepresenteerd voor toepassingen die gebruik maken van de beschreven, elektrische OPP-bron. Geïntegreerde lab-op-een-chip toepassingen, plasmonische (bio)sensoren, fotonische geïntegreerde circuits op de nanoschaal en een nieuw ontwerp voor een kwantumdot-zonnecel worden besproken.

About the author

Rob van Loon was born in Bergen op Zoom on April 7, 1981 and he was raised in the small village of Ossendrecht. In 1999, he obtained his VWO degree (pre-university education) at the "Scholengemeenschap Mollerlyceum" in Bergen op Zoom. The same year, he started his studies at the University of Twente on Applied Physics. During his studies he was an active member of the study association Arago. He performed an internship at A.D.C. Continental Temic in Lindau (Germany). The aim of his graduation project was to fabricate cavities in 3D photonic crystals and it was carried out under supervision of prof. dr. W. L. Vos at the Complex Photonics System Group. In 2004, he graduated as the first student of his year. In 2005, Rob started as a Ph.D. student at the FOM Institute for Atomic and Molecular Physics (AMOLF), under supervision of prof. dr. A. Polman. The research performed within the context of this Ph.D. project is the subject of this thesis.

Dankwoord
Acknowledgments

In deze thesis heb ik de belangrijkste resultaten van vier jaar promotie-onderzoek beschreven. Bij deze wil ik een aantal mensen bedanken die mij geholpen hebben om dit allemaal tot een goed eind te brengen.

Als eerste wil ik mijn promotor en begeleider Albert Polman hartelijk bedanken. Bedankt dat je me vier jaar terug de kans hebt gegeven om in jouw groep een boeiend onderzoek te doen en me ook veel vrijheid hebt gegeven tijdens het onderzoek. I thank Robb Walters for his enthusiasm and for his collaboration on the plasmon source project. I really enjoyed working with you and I believe I have learned quite a bit from you.

Mijn kamergenoten wil ik bedanken voor hun interesse en de discussies die al dan niet over het onderzoek gingen: René de Waele, Femius Koenderink, Ernst Jan Vesseur en Timon van Wijngaarden. De overige collega's van de groep wil ik graag bedanken voor de leuke sfeer, hun hulp en de goede discussies: Ewold Verhagen, Martin Kuttge, Erwin Kroekenstoel, Marc Verschuuren, Jeroen Kalkman, Hans Mertens, Joan Penninkhof, Sébastien Bidault en Kylie Catchpole. Petra Rodriguez, Johan Derks en Hans Zeijlemaker wil ik graag bedanken voor hun ondersteuning.

De samenwerking binnen het "Center for Nanophotonics" heb ik erg gewaardeerd. Het is een hele geschikte leerschool om goed onderzoek te doen en dit onderzoek daarna ook goed te presenteren. De colloquia waren soms zwaar, maar ze waren erg de moeite waard.

Een groot gedeelte van de samplefabricage is in het Amsterdam Nanocenter, Amolf's eigen cleanroom, gebeurd. Ik wil Chris Rétif en Hans Zeijlemaker bedanken voor hun hulp en advies om alle cleanroom technieken onder de knie te krijgen. De tekenkamer, de instrumentmakerij en de afdeling E&I wil ik

van harte bedanken voor hun ondersteuning. Met name Idsart Attema voor de elektronische ondersteuning en Jelbert Holtrop voor het stuurprogramma voor de microscoop/spectrometer. Voor het wirebonden van verschillende structuren wil ik Joop Rövekamp van het NIKHEF instituut bedanken.

Voor de depositie van SiO_x heb ik dankbaar gebruik mogen maken van de mogelijkheden in de "Surfaces, Interfaces, and Devices group" onder leiding van prof. dr. R. E. I. Schropp van de Universiteit Utrecht. Met name Eddy van Hattum en Timon van Wijngaarden wil ik hiervoor bedanken. For the deposition of Si nanocrystals in alumina, and the fabrication of the membrane structures, I thank the "Semiconductor Components Group" of the $MESA^+$-institute and the University of Twente. Ihor Brunets, Giulia Piccolo, and Jurriaan Schmitz: thanks for the pleasant collaboration. Your knowledge and expertise really made a difference.

Although at the other end of the world, I really appreciated the collaboration with Tao Lu and Kerry Vahala from the Califiornia Institute of Technology (Caltech). I enjoyed contributing to the CMOS compatible green toroid laser on silicon.

Familie en vrienden wil ik bedanken voor hun interesse en aanmoedigingen. Petra en Marijn, mijn "zusjes", bedankt dat jullie paranimf willen zijn. Succes met jullie eigen promotie. Cynthia, bedankt dat je altijd voor me klaar hebt gestaan en dat je altijd naar mijn verhaal hebt willen luisteren.

Rob.

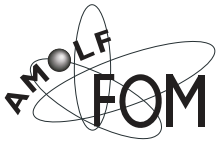

The work described in this thesis was performed at the FOM-Institute for Atomic and Molecular Physics, Kruislaan 407, 1098 SJ Amsterdam, in collaboration with Utrecht University and the University of Twente, all in the Netherlands.